

Meteorological, Impact and Climate ~~perspectives~~ Perspectives of the 29 June 2017 Heavy Precipitation Event in the Berlin Metropolitan Area

Alberto Caldas-Alvarez¹, Markus Augenstein¹, Georgy Ayzel², Klemens Barfus³, Ribu Cherian⁴, Lisa Dillenardt², Felix Fauer⁵, Hendrik Feldmann¹, Maik Heistermann², Alexia Karwat⁶, Frank Kaspar⁷, Heidi Kreibich⁸, Etor Emanuel Lucio-Eceiza^{5,9}, Edmund P. Meredith⁵, Susanna Mohr^{1,10}, Deborah Niermann⁷, Stephan Pfahl⁵, Florian Ruff⁵, Henning W. Rust⁵, Lukas Schoppa^{2,8}, Thomas Schwitalla¹¹, Stella Steidl⁷, Annegret H. Thieken², Jordis S. Tradowsky^{12,13}, Volker Wulfmeyer¹¹, and Johannes Quaas⁴

¹Institute of Meteorology and Climate Research (IMK-TRO), Karlsruhe Institute of Technology (KIT), Karlsruhe, Germany

²Universität Potsdam, Institute of Environmental Science and Geography, Karl-Liebknecht-Str. 24-25, 14476 Potsdam, Germany

³Technische Universität Dresden, Institute of Hydrology and Meteorology, Piener Straße 23, 01737 Tharandt, Germany

⁴Institute for Meteorology, Universität Leipzig, Leipzig, Germany

⁵Freie Universität Berlin, Institute of Meteorology, Carl-Heinrich-Becker-Weg 6-10, 12165 Berlin, Germany

⁶Universität Hamburg, Meteorological Institute, Grindelberg 5, 20144 Hamburg, Germany

⁷Deutscher Wetterdienst, Frankfurter Straße 135, 63067 Offenbach am Main

⁸Section Hydrology, GFZ German Research Centre for Geosciences, Telegrafenberg, 14473 Potsdam, Germany

⁹Deutsches Klimarechenzentrum, Bundesstraße 45a, 20146 Hamburg, Germany

¹⁰Center for Disaster Management and Risk Reduction Technology (CEDIM), Karlsruhe Institute of Technology (KIT), Karlsruhe, Germany

¹¹Institute of Physics and Meteorology, University of Hohenheim, Garbenstrasse 30, 70599 Stuttgart, Germany

¹²Deutscher Wetterdienst, Regionales Klimabüro Potsdam, Güterfelder Damm 87-91 14532 Stahnsdorf, Germany

¹³Bodeker Scientific, 42 Russell Street, Alexandra 9391, New Zealand

Correspondence: Alberto Caldas-Alvarez (alberto.caldas-alvarez@kit.edu) and Johannes Quaas (j.quaas@uni-leipzig.de)

Abstract. Extreme precipitation is a weather phenomenon with tremendous damaging potential for property and human life. As the intensity and frequency of such events is projected to increase in a warming climate, there is an urgent need to advance the existing knowledge on extreme precipitation processes, statistics and impacts across scales. To this end, a working group within the ~~German-based~~ Germany-based project ClimXtreme, has been established to carry out multidisciplinary analyses of high-
5 impact events. In this work, we provide a comprehensive assessment of ~~a selected case, the 29 June 2017 Heavy Precipitation Event (HPE)~~ the 29 June 2017 Heavy Precipitation Event (HPE) affecting the Berlin metropolitan region (Germany) ~~on 29 June 2017~~, from the meteorological, impacts and climate perspectives, ~~additionally estimating the contribution of climate change to its extremeness~~ including climate change attribution. Our analysis ~~shows~~ showed that this event occurred under the influence of a mid-tropospheric trough over western Europe and two short-wave surface lows over Britain and Poland (Rasmund and Rasmund II), inducing relevant low-level wind convergence
10 along the German-Polish border. ~~Several thousand~~ Over 11000 convective cells were triggered ~~in the early morning of~~, starting early morning 29 June, displacing northwards slowly under the influence of a weak tropospheric flow (10 m s⁻¹ at 500 hPa). **A**

very moist and warm southwesterly flow was present south of the cyclone over Poland, in the presence of moderate Convective Available Potential Energy (CAPE). We identified the soil in the Alpine-Slovenian region as the major moisture source for this case (63 % of identified sources). Maximum precipitation amounted to ~~The quasi-stationary situation led to totals up~~ to 196 mm d⁻¹, ~~causing the making this event the 29th most severe in the 1951-2021 climatology, ranked by means of a precipitation-based index. Regarding impacts, it incurred the largest insured losses due to a heavy precipitation event in the period 2002 to 2017 (€60 Mill.) over the area. A)~~ in the greater Berlin area. We provide further insights on flood attributes (inundation, depth, duration) based on a unique household-level ~~survey revealed that the inundation duration was 4 to 12 times larger than other surveyed events in Germany in 2005, 2010 and 2014. The climate analysis showed return periods of over~~ survey data set. The major moisture source for this event was the Alpine-Slovenian region (63 % of identified sources) ~~due to recycling of precipitation falling over that region 1 day earlier. Implementing three different Generalized Extreme Value (GEV) models, we quantified the return periods for this case to be above~~ 100 years for daily aggregated precipitation, and up to 100 years and 10 years for 8 h and 1 h aggregations, respectively. The ~~event was the 29th most extreme event in the 1951-2021 climatology in terms of severity and the second with respect to the number of convective cells triggered from 2001 to 2020 over Germany. The~~ conditional attribution demonstrated that warming since the pre-industrial era caused a small, but significant increase of 4 % in total precipitation and 10 % for extreme intensities. The ~~aerosol sensitivity experiments showed that increased anthropogenic aerosols induce larger cloud cover and probability of extreme precipitation (> 150 mm d⁻¹). Our analysis allowed relating possibility that not just greenhouse-gas-induced warming, but also anthropogenic aerosols affected the intensity of precipitation is investigated through aerosol sensitivity experiments. Our multi-disciplinary approach allowed~~ us to relate interconnected aspects of extreme precipitation. For instance, the link between the unique meteorological conditions of this case and its ~~climate extremeness~~ very large return periods, or the extent to which ~~this it~~ is attributable to already-observed anthropogenic climate change.

1 Introduction

According to the World Economic Forum Global Risks Perception Survey (Forum, 2020), extreme weather is the number one risk by likelihood and ~~among one of~~ the top four risks by impact. One of the most impactful weather types is extreme precipitation, which yearly causes local ecosystems and urban areas to suffer important damages and casualties. The probability of occurrence and magnitude of this extreme weather is projected to increase in northern and central Europe in a warming climate, as assessed by the 6th Assessment Report of the Intergovernmental Panel on Climate Change (Douville et al., 2021).

The interaction of processes across scales hampers our comprehension and prediction of Heavy Precipitation Events (HPEs). Extreme precipitation will occur only under favourable synoptic-scale conditions (Briber and Hoy, 2018) with sufficient moisture transport (Davolio et al., 2020; Caldas-Alvarez et al., 2021), and atmospheric instability (Khodayar et al., 2021), fostered by propitious phases of climate modes (Ehmele et al., 2020). This complexity is further amplified if the impacts of heavy precipitation are to be addressed. In addition to the intensity of the hazard, the impact of an event depends on the exposure and vulnerability of the affected area (Alfieri et al., 2015). This is why multidisciplinary, forensic analysis is a powerful means

45 to deal with the complex interactions underlying an HPE and its impacts. Forensic analysis consists of addressing different aspects of heavy precipitation jointly, so that the interconnections between ~~findings from different disciplines~~ different findings can be identified. For instance, Bronstert et al. (2018) investigated the Braunsbach flood in 2016, a flash flood event in a sparsely observed area, analysing the damages in the built-up area as well as its geomorphological impacts. Kunz et al. (2013) analysed Hurricane Sandy in 2012, combining an in-depth assessment of its impacts with the usage of information from
50 social networks for event reconstruction. Gochis et al. (2015) and Milrad et al. (2015) presented detailed post-event analyses using measurements, operational data products and application of models especially suited for widespread events in well-observed areas for the Colorado and Alberta floods (2013), respectively. Finally, other studies (e.g., Eden et al., 2016) have complemented forensic studies with climate change attribution experiments.

The favourable synoptic conditions for HPE development in central Europe have been assessed in previous literature. Werner
55 and Gerstengarbe (2010), using weather pattern classification, concluded that summer HPEs over Central Europe are often caused by three synoptic situations, a Trough over Central Europe (Tr), low pressure over Central Europe (TM) and a Trough over West Europe (TrW), see also Wulfmeyer et al. (2011). Brieber and Hoy (2018) found the highest probabilities for heavy precipitation events in central Germany when a TrW pattern is present, favouring the development of ~~small-scale disturbances~~ large-scale systems such as Vb-like cyclones or heat lows and prefrontal convergence zones. Depending on the location of the
60 small-scale disturbances, warm and moist air masses are transported from southern Europe towards Germany. When temperatures are already very high, the resulting increased CAPE leads to localized extreme precipitation (Bronstert et al., 2018).

A full understanding of the meteorological drivers and (small-scale) physical processes of extreme precipitation ~~is often restricted by insufficient~~ can benefit from high-resolution observations (~~Wulfmeyer et al., 2008, 2020~~) and model simulations. Numerical models offer a robust tool to simulate extreme precipitation events with fine-scale spatio-temporal detail. Further-
65 more, numerical models can also be used to create climate time series long enough to capture multi-decadal variability and numerous extreme events (Ehmele et al., 2020; Pichelli et al., 2021). Over the last decade, increased computing power has seen the growing use of kilometre-scale "storm-resolving" or convection-permitting models (CPMs; Berg et al., 2012; Barthlott and Hoose, 2015; Schwitalla et al., 2020; Stevens et al., 2020; Lucas-Picher et al., 2021), in which spatial resolution is sufficiently high ($\Delta x < 3$ km) to explicitly simulate deep convection. CPMs have thus shown added value for the simulation of sub-daily
70 extreme precipitation intensities, their spatial extent and duration, as well as their diurnal cycles (Kendon et al., 2012; Warrach-Sagi et al., 2013; Fosser et al., 2014; Stevens et al., 2020; Meredith et al., 2021). This added value offers important utility for climate-change attribution studies since CPMs give a better representation of convective extremes and are thus more reliable for detecting their climate-change response (Prein et al., 2013, 2015; Ban et al., 2021).

The impacts of extreme precipitation and the resulting pluvial flooding on society can include the loss of life, physical
75 damage to assets such as buildings or infrastructure, as well as intangible consequences such as health impacts or traffic disruptions (Merz et al., 2010; Rözer et al., 2016). The impacts depend on the hazard intensity, the exposed assets and their vulnerability (Kron, 2005). The hazard level itself is a function of meteorological factors, e.g. precipitation intensity or affected area. The exposure and vulnerability depend on aspects such as the inundation depth, the topography, the degree of sealing of

surfaces, or the sewer system capacity (Kron, 2005; Smith et al., 2015). ~~Hence, whether a flood causes damage depends not only on the development of a meteorological situation, but also on the number and types of exposed assets and their vulnerability.~~

To analyse the associated impacts, not only meteorological data is crucial, but also targeted information collected during or after an event, e.g. damage to buildings and contents. Such data can be collected, for example, through surveys of affected households or through assessments by loss surveyors during insurance claim validation (Spekkers et al., 2014, 2017; Van Ootegem et al., 2015, 2018; Rözer et al., 2019). However, when analysing damage records, it is important to consider that results depend on how the affected society understands, records, and remembers those impacts (Kuhlicke et al., 2020). The case under study here, the 29 June 2017 ~~event~~ HPE in the metropolitan Berlin area (Germany), has been investigated before based on survey data of affected households in Berlin-Brandenburg. Berghäuser et al. (2021) and Dillenardt et al. (2021) addressed the tangible and intangible consequences of extreme precipitation and associated pluvial flooding for households for this event, respectively, but a focused analysis comparing its impacts to those of similar HPEs in the climatology is still lacking.

From the climate perspective, information on how the frequency of HPEs has changed in the recent climate is demanded by interested stakeholders. This can be provided through estimation of probabilities of exceedance or return periods for specific events. Generalized Extreme Value (GEV) models can be fitted to a climate observational precipitation dataset to derive this information (Wilks, 2006). Previous studies have provided estimations of return periods for similar events, finding extreme values of over 200 years for the Seine river flooding (France) in 2016 (Philip et al., 2018), the Braunsbach flooding (southern Germany) in 2016 (Piper et al., 2016) and the three-week flooding in Germany in 2018 (Mohr et al., 2020). The flooding in July 2021 in the Ahr, Erft and Meuse rivers, was analysed by Kreienkamp et al. (2021), who found that an event of similar meteorological characteristics can be expected in the present climate in Central Europe once every 400 years.

Also at the climate scale, extreme event attribution has proven useful to estimate how the severity and/or likelihood of an event has been affected by anthropogenic influences (Allen, 2003; Stott et al., 2004; Otto, 2017). Anthropogenic influence typically refers to climate change, but could also include, e.g., land-use changes (Sebastian et al., 2019) or changes in atmospheric pollutants (Liu et al., 2020). To this end there are two mainly-used approaches. The first approach is probabilistic event attribution, which consists of simulating how the dynamics of the climate system evolve under climate change. It can therefore be used to detect significant changes in the severity and frequency of extreme events. This technique, however, is applicable to model data with a relatively coarse resolution and is, therefore, best suited for attribution studies of large-scale events. The second approach is conditional event attribution (Trenberth et al., 2015), which evaluates to what extent observed climate change may have impacted the magnitude of an event. The attribution is thus conditional on the presence of a given dynamical situation, and implies that thermodynamic changes due to climate change have been demonstrated. However, a limitation of this approach is that changes in the probability of the event's underlying dynamical situation cannot be determined.

The research presented here has been carried out in the framework of the Germany-based project Climate change and eXtreme events (ClimXtreme¹), which brings together governmental and research institutions in the fields of atmospheric physics, statistics, impact studies and computing. ~~ClimXtreme deals with the influence of climate change on atmospheric~~

1

~~extremes. To facilitate reproducibility and cooperation between project members, ClimXtreme uses~~ This framework facilitates the multi-disciplinary approach of this study, where in addition to the usual communication and collaboration tools, the ClimX-
115 ~~treme Central Evaluation System (XCES), a scientific software infrastructure (Kadow et al., 2021) that allows (Kadow et al., 2021)~~ has allowed centralized consultation and analysis of all the data within the project.

The aim of this study is to provide a comprehensive assessment of the 29 June 2017 HPE in the area of Berlin (Germany) from the meteorological, impacts and climate ~~perspective, additionally estimating the contribution of climate change to its extremeness~~ perspectives, including climate change attribution. The paper is structured as follows: in ~~Section~~ Sect. ??
120 ~~2~~ we present the ~~datasets and methods used for analysis. In Section 4 we describe our results from the multidisciplinary analyses. Finally, in~~ observational and modelling datasets used, in Sect. 3, the particular techniques and methodologies used are introduced. Section 4 shows the main analyses and outcome of our work and in Sect. 5 we ~~introduce our conclusions, findings present our conclusions~~ and outlook.

2 Data ~~and methods~~sets

125 2.1 ~~Atmospheric observations and reanalyses~~Observations

~~Our analysis is based on precipitation, lightning and survey observations. Where observations were not available, we utilize climate reanalyses.~~

2.1.1 ~~Precipitation~~

REGIONalisierte NIEederschlaege (REGNIE)

130 REGNIE is a gridded data set of 24-hour totals (from 06 UTC to 06 UTC) based on approximately 2,000 rain gauges distributed across Germany. A post-processing is applied to station data for regridding to a $1 \times 1 \text{ km}^2$ mesh taking into account elevation, exposure and climatology, avoiding smoothing observed precipitation extremes (Rauthe et al., 2013; Hu and Franzke, 2020). The data are provided by the German ~~Weather Service (~~Meteorological Service (Deutscher Wetterdienst, DWD) from 1951 for all of Germany (for the former West Germany, the daily values are available since 1931). The long-term availability of
135 REGNIE is its main advantage for climate studies.

~~a) Spatial extent of the used data sets REGNIE, RADKLIM, COSMO-REA6, WRF-1.5km, ICON-625m and COSMO-CLM-2.8.
b) Close-up view of Berlin and surroundings, as well as the DWD stations used for validation (crosses), the location of surveyed events from Table 1 (red dots) and the Berlin-Tempelhof station analysed in Figure 11 (blue dot), Basemap: Global Land One-kilometer Base Elevation (GLOBE) (Hastings et al., 1999).~~

140

RADar KLIMatologie (RADKLIM)

RADKLIM is a precipitation climate data set derived from the C-band radar network (17 radar sites) operated by DWD. The data set comprises two products; the gauge-adjusted one-hour precipitation sum (RW) and the quasi gauge-adjusted five-

minute precipitation rate (YW), with $1 \times 1 \text{ km}^2$ resolution. The data are post-processed using the Radar-Online-Aneichung (RADOLAN) method, correcting existing artifacts by adjusting precipitation sums from the radar with precipitation measurements from rain gauge stations (Bartels et al., 2004). Due to the dense spatial and temporal resolution, RADKLIM detects short-term, convective extreme intensities frequently missed by station data (Lengfeld et al., 2020; Winterrath et al., 2017). ~~It is available between 2001 and 2020.~~

150 Deutscher Wetterdienst (DWD) stations

Daily precipitation measurements from the DWD high-density network were used as reference. The data are quality controlled, but a continuous homogenization is not applied. Hence, the data could be subject to partial inhomogeneities, such as station relocations or changes in the instrumentation (Kaspar et al., 2013). The DWD high-density network has a high accuracy and resolution (Kaspar et al., 2013) and therefore we select it for validation. Nonetheless, this dataset is used for deriving the REGNIE gridded product and for adjusting RADKLIM which makes these data sets dependent. We concede this dependency to profit from the best rain gauges product available in the region.

European Cooperation for Lightning Detection (EUCLID)

The lightning activity in and around Berlin is investigated with data from the ground-based low-frequency lightning detection system European Cooperation for Lightning Detection (EUCLID) network, which covers the whole European continent (Drüe et al., 2007; Schulz et al., 2016; Poelman et al., 2016). Cloud-to-ground strokes are used to illustrate the temporal development of convective activity during the extreme event, similar to Piper and Kunz (2017) and Wilhelm et al. (2021). The spatial resolution of EUCLID has been improved to less than 90 m in the year 2016 due to algorithm optimizations (Schulz et al., 2016).

165 **CATalogue of Radar-based heavy Rainfall-Events (CatRaRE)**

The RADKLIM data set at 1 h and $1 \times 1 \text{ km}^2$ km resolution (RW) was used as the basis to derive an HPE catalogue for Germany (CatRaRE) for the period 2001 to 2020. Here we use Version 2017.002 (Lengfeld et al., 2021a, b), including precipitation sums with 11 different accumulation periods (1, 2, 3, 4, 6, 9, 12, 18, 24, 48 and 72 hours). For each duration and time step, extreme events are detected based on the DWD Warning Level (WL) 3 for severe weather, or if they have a return period of 5 years. The duration in hours, the affected area in km^2 , the location (county and community), the maximum and mean precipitation amount in mm as well as affected residents in the event area and further meta information is included.

2.1.1 Lightning data

~~The lightning activity in and around Berlin is investigated with data from the ground-based low-frequency lightning detection system operated by Siemens as part of the European Cooperation for Lightning Detection (EUCLID) network, which covers the whole European continent (Drüe et al., 2007; Schulz et al., 2016; Poelman et al., 2016). Cloud-to-ground strokes are used to illustrate the temporal development of convective activity during the extreme event, similar to Piper and Kunz (2017) and~~

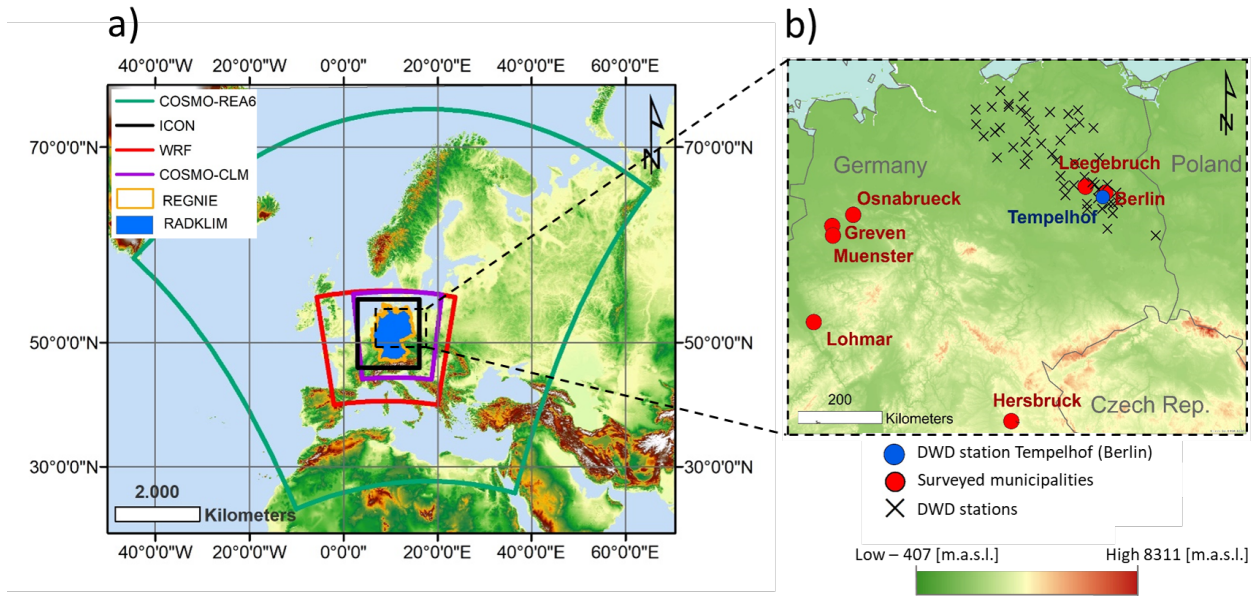


Figure 1. a) Spatial extent of the used data sets REGNIE, RADKLIM, COSMO-REA6, WRF-1.5km, ICON-625m and COSMO-CLM-2.8. b) Close-up view of Berlin and surroundings, as well as the DWD stations used for validation (crosses), the location of surveyed events from Table 1 (red dots) and the Berlin-Tempelhof station analysed in Figure 11 (blue dot). Basemap: Global Land One-kilometer Base Elevation (GLOBE) (Hastings et al., 1999).

Wilhelm et al. (2021). The spatial resolution of EUCLID has been improved to less than 90 m in the year 2016 due to algorithm optimizations (Schulz et al., 2016).

2.1.1 Reanalyses

180 2.2 Reanalyses

ERA5

ERA5 data are used to identify and track the low pressure systems, find moisture sources and force numerical simulations. This is the fifth generation of the European Center for Medium-Range Weather Forecasts' (ECMWF) atmospheric reanalysis of the global climate (Hersbach et al., 2020). It has a spatial resolution of $31 \times 31 \text{ km}^2$ and is available from 1950 to present at hourly resolution. ERA5 is based on the Integrated Forecasting System (IFS) and uses a 4D-Var assimilation scheme, assimilating different observation types. ERA5 has demonstrated a good performance in representing heavy precipitation (Keller and Wahl, 2021).

2.3 Validation of precipitation data sets

190 To ensure consistency of our results, we provide a quantitative validation of the used precipitation products and of ERA5. REGNIE, RADKLIM and ERA5 are compared pointwise (by selecting the nearest neighbour grid cell) to observations made at 53 DWD stations, located in the area (Fig. 1b). Additionally, the regional reanalysis Consortium for Small-Scale Modeling – Reanalysis 6 km (COSMO-REA6
COSMO-REA6) is compared (Bollmeyer et al., 2015) to provide a reference for ERA5 with another reanalysis product.
195 COSMO-REA6 was developed by the [is a regional reanalysis product for the European CORDEX domain, developed by University of Bonn and the DWD within the Hans-Ertel-Centre for Weather Research \(Simmer et al., 2016\)](#). It has about 6×6 km² [a 6 x 6 km](#) horizontal resolution and accumulated precipitation is provided hourly (Bollmeyer et al., 2015).

Daily precipitation measurements from the DWD high-density network were used as reference. The data are quality controlled, but a continuous homogenization is not applied. Hence, the data could be subject to partial inhomogeneities, such as station
200 relocations or changes in the instrumentation (Kaspar et al., 2013). The DWD high-density network has a high accuracy and resolution (Kaspar et al., 2013) and therefore we select it for validation. Nonetheless, this dataset is used for deriving the REGNIE gridded product and for adjusting RADKLIM which makes these data sets dependent. We concede this dependency to profit from the best rain gauges product available in the region.

In the validation, different scores are computed based on daily precipitation sums over the years 2001 to 2018, which is
205 the longest period for which all data sets are available. We compute absolute frequencies (Fig. 2.a), the Symmetric Extremal Dependency Index (SEDI; Fig. 2.b) and the frequency bias (Fig. 2.c). The absolute frequencies show the number of days with a specific amount of precipitation for each data set. The SEDI estimates the dependency between an event in the given data set and the reference observations (Ferro and Stephenson, 2011). Finally, the frequency bias describes the ratio between the number of events in the data sets and the reference observations (Hogan et al., 2009). The evaluations are made for three
210 precipitation intervals based on the WLs used operationally by the DWD, namely WL2 (> 30 mm), WL3 (> 50 mm) and WL4 (> 80 mm). The observed 29 June event falls into the WL4 category.

Evaluation of daily precipitation estimates from REGNIE, RADKLIM, ERA5 and COSMO-REA6 compared with DWD station observations (see Fig. 1.b). The selected period is 2001 to 2018, using the nearest neighbour grid cells to the DWD stations. (a) Histogram showing the absolute occurrences of precipitation within WLs 2, 3 and 4, (b) Symmetric Extremal
215 Dependency Index (SEDI) and (c) frequency bias. Positive (negative) frequency bias indicates an overestimation (underestimation) of events, the black horizontal line represents the optimum value.

REGNIE fits best the observations for absolute frequency (37 events in REGNIE, 34 in the DWD stations at WL4), followed by RADKLIM (24 events in WL4) and ERA5 (Fig. 2.a). The latter only has 12 events (WL4), which is probably due to its coarse resolution and the inability to explicitly resolve structures smaller than 25×25 km². This impact of model resolution is further
220 evidenced by the performance of the second reanalysis [is available from Jan 1995 to Aug 2019. It is based on the NWP-system COSMO and uses a nudging scheme for data assimilation. Subgrid-scale convection is parameterized with the Tiedtke scheme \(Tiedtke, 1989\) and precipitation from meteorological stations or radar is not assimilated \(Bollmeyer et al., 2015\)](#). COSMO-

225 REA6 with 36 events in WL4. Despite both reanalyses using deep convection parameterizations, COSMO-REA6 is able to represent larger precipitation intensities and hence more HPEs. Regarding SEDI, REGNIE again compares best with station observations, also followed by RADKLIM (Fig. 2b). In contrast, the coarser reanalysis products show lower, but acceptable values, especially for WL4. Finally, for frequency bias, REGNIE shows no deviations, RADKLIM has a negative bias, i.e. less events detected, and ERA5 performs poorly for all WLS. has shown low biases for extreme precipitation compared to other reanalysis products (Keller and Wahl, 2021).

230 We conclude that REGNIE and RADKLIM are well suited for process-based and statistical analyses of extreme precipitation at the meteorological and climate scales and that ERA5 performed badly in the comparison against the DWD stations. However, the good results of ERA5 in SEDI for extreme events (WL4; Fig. 2.b) and the accuracy shown by previous studies for large-scale precipitation and relevant atmospheric variables (Martens et al., 2020; Hersbach et al., 2020; Yu et al., 2021) render this product suitable for the applications of this study. Here we use ERA5 to assess the large-scale conditions of moisture transport (Fig. 9).

235 2.3 Convection Permitting Models

2.4 Simulations

~~We use CPM simulations when observations are nonexistent or lowly resolved, as well as for sensitivity experiments.~~

2.3.1 **Convection-permitting Weather Research and Forecasting (WRF) simulation for process-understanding**

Weather Research and Forecasting (WRF)

240 WRF model version 4.2.1 (Skamarock et al., 2021) at a convection permitting resolution of 1.5 km with 100 vertical levels is used. The model domain covers central Europe (Fig. 1a) and the simulation was initialized with the operational ECMWF analysis at 00 UTC on 29 June 2017 (12 hours before the event). Lateral boundary conditions were provided every 6 hours. The ~~set up~~ setup of the physical parametrizations is similar to Schwitalla et al. (2021) except that 1) the Mellor–Yamada–Nakanishi–Niino (MYNN) planetary boundary layer parametrization (Nakanishi and Niino, 2006, 2009; Olson et al., 2019) is applied, and 2) 245 the microphysics scheme of Thompson and Eidhammer (2014) (~~FE2014~~) is used. Land cover maps have been updated using the high-resolution European Space Agency Climate Change Initiative (ESA CCI) data set (ESA, 2017). In addition, the green vegetation fraction and leaf area index (LAI) have been adjusted for 2017 by means of the Copernicus Global Land Service portfolio 1 km resolution data sets (<https://land.copernicus.eu/global/>). Finally, high-resolution soil texture data from Poggio et al. (2021) (<https://soilgrids.org>) were used.

250

2.3.1 **Convection-permitting COSMO-CLM simulations for conditional attribution**

Consortium for Small Scale Modelling in CLimate Mode (COSMO-CLM)

For the conditional climate change attribution experiment (Sect. ??), high-resolution ensembles (17 members) of the event under present and pre-industrial conditions are simulated with the COSMO model in CLimate Mode (COSMO-CLM; Rockel et al., 2008). For the present climate, ERA5 reanalysis (Hersbach et al., 2020) is dynamically downscaled to 0.11° for 17 members over a pan-Europe domain (Fig. S4) using the domain-shift ensemble technique (e.g. Rezacova et al., 2009; Noyelle et al., 2019). All members are then further dynamically downscaled to a COSMO-CLM version 5.0_cml6 is run at a convection-permitting resolution of 0.025° resolution over a fixed. The model has $461 \times 421 \times 50$ sub-domain. To create the pre-industrial ensemble, the warming signal since the pre-industrial period, here taken as 1850–1859 versus 2007–2016 (over the gridpoints (lat/lon/height), a model top at 22.7 km and a relaxation zone of 50 km. Hourly lateral boundary conditions include cloud ice, cloud water and cloud graupel, and are provided by ERA5-forced 0.11° domain), is first computed from a subset of 17 Coupled Model Interecomparison Project Phase 6 simulations (CMIP6) models (O’Neill et al., 2016). The warming signal (Fig. 12a) is then subtracted from the ERA5 initial and boundary conditions of the 0.11° simulations (surface temperatures are modified based on the warming signal at the lowest model level). A similar procedure is repeated for soil temperature. The atmospheric moisture content is adjusted based on the assumption that relative humidity remains constant. Pressure at the COSMO-CLM height levels is adjusted by numerically integrating the hydrostatic balance equation downwards from the model top (Kröner, 2016). The 0.11° and 0.025° simulations are initialized on 28 June at 12:00 and 23:00 UTC, respectively, giving sufficient spin-up and adjustment time prior to the analysis period of 07:00 to 22:00 UTC the following day (chosen based on the analysis in Fig. S5). The attribution analysis consists of comparing the precipitation between the 0.025° ensembles with the pre-industrial ensemble as the reference state. COSMO-CLM model settings are as described in Meredith et al. (2021). Further details of the simulations and the CMIP6 models can be found in the supplementary material Section 3.6). Deep convection is treated explicitly and shallow convection is parametrized with a modified Tiedtke scheme (Tiedtke, 1989). A full description of all model physics is found in Baldauf et al. (2011).

2.3.1 Sub-kilometre ICON simulations for aerosol sensitivity experiments

Simulations with the Icosahedral Non-hydrostatic (ICON) atmospheric model were conducted to examine the possible role of anthropogenic aerosols in the analysed event. The model domain covered central Europe (Fig. 1), for which one-way-nested simulations at resolutions of 625 m and 1.25 km, respectively, are produced with 90 vertical levels. The model setup otherwise follows Costa-Surós et al. (2020). The simulation was

Icosahedral Non-hydrostatic Model (ICON)

The ICON simulations follow Costa-Surós et al. (2020) and were initialized with the operational ECMWF analysis (IFS data) at 00 UTC on 29 June 2017 and lateral boundary conditions are provided every 6 h. For analysis, the daytime period between 06:00 and 20:00 UTC is chosen. In order to assess the role of cloud-active aerosols in the 2017 event, two simulations are carried out with two different imposed concentrations of cloud condensation nuclei, i. e. one with low concentrations, corresponding to current conditions (CLN), and one with elevated aerosol concentrations (POL), corresponding approximately the peak aerosol concentrations over Central Europe observed in the mid-1980s.

3 Methods

Our forensic study analysis, statistical and computational methods of meteorological, climate and impact studies to provide the full picture on the case. In these methods are introduced and details can be found in the referenced literature.

3.1 The Precipitation Severity Index (PSI)

290 We use the Precipitation Severity Index (PSI; Caldas-Alvarez et al., 2022) to detect extreme precipitation events according to three different but complementary characteristics of heavy precipitation: intensity, spatial extent and persistence. The PSI in its current form is an adaptation of the Storm Severity Index (SSI; Leckebusch et al., 2008; Pinto et al., 2012) and is a unitless index that indicates the degree of daily precipitation severity with respect to a predetermined climatological threshold (in our case the 80th percentile). Large PSI values represent high intensity, geographically extensive and temporally persistent
295 precipitation events.

3.2 Lagrangian convective cell tracking

We perform Lagrangian convective cell tracking for the years 2001 to 2020 for a region of 200 x 200 km centered over Berlin. Pixels of YW RADKLIM radar data exceeding a threshold of 8.12 mm/h were identified as convective cells (Purr et al., 2021). The displacement of the cell is projected applying the 700 hPa wind of ERA5. If in the consecutive timestep a convective cell
300 has been found in the area defined by a search radius around the projected position, both cells are assigned to the same cell track. If multiple cells are found within the search radius, the cell with the minimum distance is assigned to the cell track.

3.3 Lagrangian moisture backward trajectories

We calculate Lagrangian backward trajectories following Sodemann et al. (2008), based on ERA5 reanalysis data (Hersbach et al., 2020), in a mid-European region around the center of maximum precipitation (red box in Fig. 9). We start the trajectories from
305 1000 hPa to 200 hPa in steps of 50 hPa for every hour of 29 June 2017, with a horizontal grid spacing 80 km and going back 240 h in time. From all trajectories, we selected those that have a relative humidity of at least 80 % in the target box and for which the specific humidity decreases during the last time step (precipitation) (Sodemann et al., 2008; Grams et al., 2014). Along each selected trajectory, moisture uptake has been computed based on hourly specific humidity increases in the planetary boundary layer associated with evapotranspiration from the surface. The boundary layer height is available as a diagnostic
310 model variable in the ERA5 data set and, again following Sodemann et al. (2008), is multiplied by a factor of 1.5 to account for potential uncertainties in this diagnostic estimate. These uptakes have been weighted according to their contribution to the precipitation (moisture loss) at the target location, taking into account that earlier moisture uptake may contribute less due to precipitation loss on their way to the target region.

3.4 ~~Impacts and losses~~ Household surveys for impact evaluation

315 To assess the overall losses caused by the 29 June 2017 event, ~~we reviewed HPE~~, we review reports from the German Insurance Association (GDV), which published loss estimates for severe extreme precipitation events in Germany in the period 2002-2019 (GDV, 2018, 2020, 2021), and other technical reports (Hydrotec et al., 2008). At the household level, we ~~used~~ use losses, flood-duration and flood-depth data derived from household surveys in Berlin and Brandenburg (Dillenardt et al., 2021). We furthermore ~~used~~ use survey data from private households in Hersbruck (affected in 2005), Lohmar (affected in 320 2005), Osnabrueck (affected in 2010) (Rözer et al., 2016) and Muenster (affected in 2014) (Spekkers et al., 2017). In the surveys, affected households were asked, inter alia, when they were last affected by heavy rain and what impact they suffered. The results of the surveys are based on the responses of those households and are thus subjective.

3.5 Generalized Extreme value-Value (GEV) statistics

~~Extreme value theory is used to analyse or statistically model extreme values of a data set. A probability distribution function is fitted to a sample of extreme events. This allows a probability of exceedance p for a given threshold R , e.g. a rainfall total, to be computed and expressed as a return period t_{RP} using $t_{RP} = 1/p$. For example, a probability of exceedance $p = 0.01$ for annual data can be interpreted as on average 1 event in 100 years.~~

~~In order to estimate these values reliably, a trade-off has been made in the past between the simplicity of a method, the return period size and the computational effort (Svensson and Jones, 2010). In hydrometeorology, block maxima using the GEV have been widely adopted to estimate return periods (Wilks, 2006; Svensson and Jones, 2010). Often the special case, the type I distribution, also known as the Gumbel distribution (Extreme Value Type~~ The standard GEV distribution applied to heavy precipitation in this work is given by Coles (2001):

$$G(R) = \exp \left(- \left\{ 1 + \xi \left(\frac{R - \mu}{\sigma} \right) \right\}^{-1/\xi} \right), \quad (1)$$

~~where μ denotes the location parameter, σ the scale ($\sigma > 0$) and ξ the shape parameter. A special case of the standard distribution (Eq. 1), has been used (e.g. Grieser et al., 2007; Svensson and Jones, 2010; Van den Besselaar et al., 2013; Maity, 2018; Piper 1) is the Type I or Gumbel distribution (Gumbel, 1958) obtained in the limit $\xi \rightarrow 0$ used as well in previous works (e.g. Grieser et al., 2007; 335~~

$$F(R) = \exp \left(- \exp \left(\frac{\mu - R}{\sigma} \right) \right). \quad (2)$$

~~This simplification allows estimation of the two free GEV parameters μ and σ by means of the Method of Moments, which is less computationally intensive and has been proven useful in the past (e.g. Svensson and Jones, 2010; DWA, 2012; Piper et al., 2016) . Characteristic of the Gumbel distribution is an exponential decay of the probability density function, meaning that only two free parameters of the GEV-fit have to be estimated. However, the Gumbel is not a heavy-tailed distribution and is characterised by constant skewness and kurtosis.~~

The ~~We fit~~ block maxima series ~~are to Eqs. 1 and 2~~ obtained by splitting the sample into non-overlapping intervals of the same size and then taking the maximum value of each interval. Previous studies have demonstrated that the annual block maxima approach is suitable for mid-latitude precipitation series (Kharin and Zwiers, 2000; Rust, 2009). ~~The GEV distribution is given by Coles (2001):-~~

$$G(R) = \exp \left(- \left\{ 1 + \xi \left(\frac{R - \mu}{\sigma} \right) \right\}^{-1/\xi} \right),$$

where μ denotes the location parameter, σ the scale ($\sigma > 0$) and ξ the shape parameter. In the limit $\xi \rightarrow 0$, we obtain the special case Gumbel distribution (Gumbel, 1958):-

$$F(R) = \exp \left(- \exp \left(\frac{\mu - R}{\sigma} \right) \right).$$

This simplification allows estimation of the two free GEV parameters μ and σ by means of the Method of Moments, which is less computationally intensive and has been proven useful in the past (e.g. Svensson and Jones, 2010; DWA, 2012; Piper et al., 2016). Return values RV_{RP} (quantiles) and the associated return periods t_{RP} , or directly the probability of exceedances p , are related to the GEV distribution as $t_{RP} = 1/(1 - G(RV_{RP}))$ (Coles, 2001). Thus, once μ and σ are estimated from the data, the return periods can be directly derived from the extreme value models with Equations 1 and 2.

Additionally, we ~~We~~ specify the uncertainty of the models by using 95 % confidence intervals obtained from 1000-fold bootstrapping (re-sampling with replacement) from the maxima series of the original data set (Efron and Tibshirani, 1993), following the ordinary non-parametric bootstrap percentile method of Mélése et al. (2018). From these 1000 samples the 2.5 % and 97.5 % quantiles of the wanted property (either return periods or return values) indicate their confidence boundaries.

~~A We further implement a duration-dependent (d-GEV) model with 7 parameters, which covers different durations to achieve a more efficient usage of observations could improve the estimation of return periods. This can be achieved by including precipitation maxima of different accumulation durations d. This. This~~ way, information about short time scales (minutes to hours), ~~for which observational records are typically short,~~ can be derived, to a certain extent, from information of longer time scales (hours to days) ~~by using the duration-dependency between time scales. Equation 1 is adapted to be duration-dependent (d-GEV) with 7 parameters, which covers the full range of durations considered.~~ Duration-dependency is incorporated into the GEV in order to reduce assumptions about the underlying distribution and have a free shape parameter ξ in the GEV (Coles, 2001). Another reason for using the GEV instead of one of their special cases, is that Gumbel, as well as the other two GEV special cases Fréchet and Weibull, require large data sets to fulfil the limiting theorem for large block sizes (Papalexiou and Koutsoyiannis, 2013). The d-GEV includes all three types and is a good choice if block size does not reach the asymptotic regime required for Gumbel. A duration-dependent GEV (d -GEV) as suggested by Koutsoyiannis et al. (1998) and refined by

Fauer et al. (2021) is introduced by varying the characteristic parameters of the GEV:

$$G_d(R; d) = \exp \left(- \left\{ 1 + \xi \left(\frac{R - \mu(d)}{\sigma(d)} \right) \right\}^{-1/\xi} \right), \quad (3)$$

$$\sigma(d) = \sigma_0(d + \theta)^{-(\eta_1 + \eta_2)} + \tau,$$

$$\mu(d) = \tilde{\mu}(\sigma_0(d + \theta)^{-\eta} + \tau),$$

$$\xi = \text{const.},$$

where $\tilde{\mu}$ is the re-scaled location parameter, σ_0 is the scale offset, θ is the duration offset, η_1 and η_2 are duration exponents and τ is the intensity offset. Parameters were estimated with Maximum Likelihood Estimation (MLE), a flexible and efficient parameter estimation method which is known to provide asymptotically unbiased and smallest-possible variant estimates (Coles, 2001; Davison and Huser, 2015). However, MLE is more computationally expensive than the method of moments. Jurado et al. (2020) justified the use of the MLE for duration-dependent extreme precipitation studies as the explicit consideration of the dependence between durations in a model leads to only marginal differences in estimation. The d -GEV has been recently applied successfully by Ulrich et al. (2020).

3.6 Conditional event attribution with CPM

For the conditional climate-change attribution experiment (Section 4.4), high-resolution ensembles (17 members) of the event under present and pre-industrial conditions are simulated with the COSMO-CLM (Rockel et al., 2008). For the present climate, ERA5 reanalysis (Hersbach et al., 2020) is dynamically downscaled to 0.11° for 17 members (Fig. S3) using the domain-shift ensemble technique (e.g. Rezacova et al., 2009; Noyelle et al., 2019). All members are then further dynamically downscaled to a convection-permitting 0.025° resolution over a geographically-fixed sub-domain (see Section 2.3.1). To create the pre-industrial ensemble, the warming signal since the pre-industrial period, here taken as 1850-1859 versus 2007-2016 (over the 0.11° domain), is first computed from a subset of 17 Coupled Model Intercomparison Project Phase 6 (CMIP6) models (O'Neill et al., 2016). The warming signal (Fig. 12a) is then subtracted from the ERA5 initial and boundary conditions of the 0.11° simulations (surface temperatures are modified based on the warming signal at the lowest model level). A similar procedure is repeated for soil temperature. The atmospheric moisture content is adjusted based on the assumption that relative humidity remains constant. Pressure at the COSMO-CLM height-levels is adjusted by numerically integrating the hydrostatic balance equation downwards from the model top (Kröner, 2016). The 0.11° and 0.025° simulations are initialized on 28 June at 12:00 and 23:00 UTC, respectively, giving sufficient spin-up and adjustment time prior to the analysis period of 07:00 to 22:00 UTC the following day (chosen based on the analysis in Fig. S4). The attribution analysis consists of comparing the precipitation between the 0.025° ensembles with the pre-industrial ensemble as the reference state. COSMO-CLM model settings are as described in Meredith et al. (2021). Further details of the simulations and the CMIP6 models can be found in the supplementary material.

3.7 Aerosol sensitivity experiments

405 Simulations with the ICOSahedral Non-hydrostatic (ICON) atmospheric model were conducted to examine the possible role of anthropogenic aerosols in the analysed event. The model domain covered central Europe (Fig. 1), for which one-way nested simulations at resolutions of 625 m and 1.25 km, respectively, are produced with 90 vertical levels. Two hectometer ICON simulations at are carried out with two different imposed concentrations of cloud condensation nuclei, i.e. one with low concentrations, corresponding to current conditions (CLN), and one with elevated aerosol concentrations (POL), corresponding approximately to the peak aerosol concentrations over Central Europe observed in the mid-1980s.

4 Results

410 4.1 Meteorological situation

415 Provided our multi-disciplinary approach, we need to verify that there are no inconsistencies among the different datasets used. To reduce this uncertainty we need to ensure that all of them represent a similar climatology of heavy precipitation in the region. To this end, we provide a quantitative validation of the products REGNIE, RADKLIM, ERA5, and COSMO-REA6 for the period 2001-2018. We compare these datasets pointwise (by selecting the nearest neighbour grid cell) to observations made at 53 DWD stations (Sect. 2.1.1; Fig. 1). COSMO-REA6 is included in this comparison to provide a reference for ERA5 with another reanalysis product. We compute absolute frequencies, as the number of days with a specific amount of precipitation for each data set; the Symmetric External Dependency Index (SEDI), estimating the dependency between an event in the given data set and the reference observations (Ferro and Stephenson, 2011); and the frequency bias as the ratio between the number of events in the data sets and the reference observations (Hogan et al., 2009). The evaluations are made for three precipitation intervals based on the warning levels used operationally by the DWD, namely WL2 (> 30 mm), WL3 (> 50 mm) and WL4 (> 80 mm). The 29 June 2017 HPE falls into the WL4 category.

420 REGNIE, RADKLIM and COSMO-REA6 perform well, in representing the climatology of extreme precipitation (WL4 category). In particular, REGNIE fits best the DWD station observations for absolute frequency (37 events in REGNIE, 34 in the DWD stations at WL4), followed by RADKLIM (24 events in WL4). ERA5 (Fig.2.a) only has 12 events (WL4). Regarding SEDI (Fig. 2.b), REGNIE again compares best with station observations, also followed by RADKLIM (Fig. 2b) in contrast to the coarser resolution reanalysis products which show lower SEDI values. However their performance is better for extreme precipitation (WL4). Finally, for frequency bias, REGNIE shows no deviations, RADKLIM has a negative but acceptable bias, i.e. less events detected, and ERA5 performs poorly for all WLS.

430 To summarize, we find a good agreement of REGNIE and RADKLIM with the DWD station observations which gives us confidence that their representation of HPEs will be consistent. ERA5, however showed a bad performance for absolute and frequency bias and the moderate precipitation categories (WL2 and WL3) for SEDI. The performance of ERA5 was worse than the other reanalysis product, COSMO-REA6, possibly due to their difference in model resolution. For this reason ERA5 will not be used hereafter to study heavy precipitation fields. Its use will be restricted to other relevant large-scale atmospheric fields such as water vapour (Fig. 9).

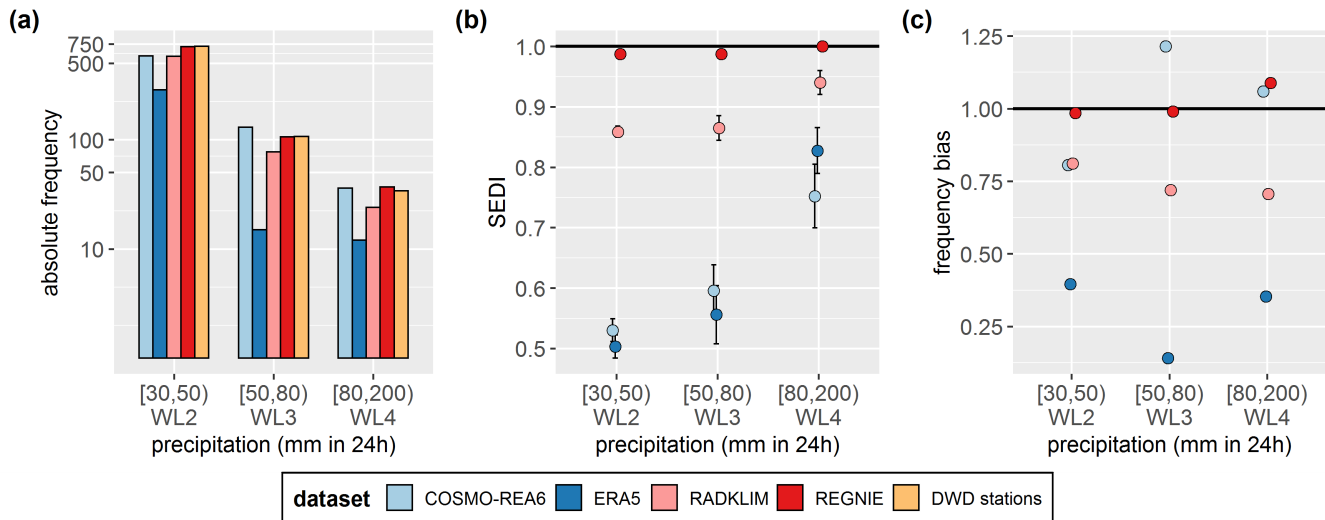


Figure 2. Evaluation of daily precipitation estimates from REGNIE, RADKLIM, ERA5 and COSMO-REA6 compared with DWD station observations (see Fig. 1.b). The selected period is 2001 to 2018 (concurrent period of data availability), using the nearest neighbour grid cells to the DWD stations. (a) Histogram showing the absolute occurrences of precipitation within WLs 2, 3 and 4, (b) Symmetric Extremal Dependency Index (SEDI) and (c) frequency bias. Positive (negative) frequency bias indicates an overestimation (underestimation) of events, the black horizontal line represents the optimum value.

435 4.1 Event analysis and climate context

The 29 June 2017 HPE occurred under the influence of an upper-level trough over western Europe extending between the Iberian Peninsula and Poland (TrW pattern), present between 28 June and 01 July, with. During this period, several short-wave surface lows developing developed on the northern side of the trough (Fig. ??). At 12 UTC (29 June), the core of the low-pressure was located between France and the British Isles showing relative topography values of 550 dam between 1000 hPa and 500 hPa (Fig. ??). Close to the ground, the interaction between two 3.a) inducing favourable conditions for convective development. Two small-wave surface lows caused most of the precipitation collected over Berlin during 29 June. The first system, named Rasmund, remained quasi-stationary east of the British Isles between 28 June and 01 July, reaching values of the Pressure at the Mean Sea Level (PMSL) of 994 hPa (Fig. ??). This system originated from two converging surface lows coming from the Atlantic Ocean and France, respectively. 3.a). The second surface low, Rasmund II, originated in the night of 445 from 28 to 29 June over central Europe (Czech Republic), displaced towards northern Poland over the course of 6 h, and showed PMSL of 990 hPa along the German-Polish border at 12 UTC (29 June). The cyclonic circulations of both surface lows caused convergence of cold air masses from the Atlantic with the warm and wet air masses from southern Europe (Gebauer et al., 2017).

Figure ?? provides further insights into the evolution of the event based on the operational ECMWF analysis. The mesoscale circulation associated with the mid-tropospheric low Rasmund II over northern Poland (550 dam; Fig. ??a) shows a westerly

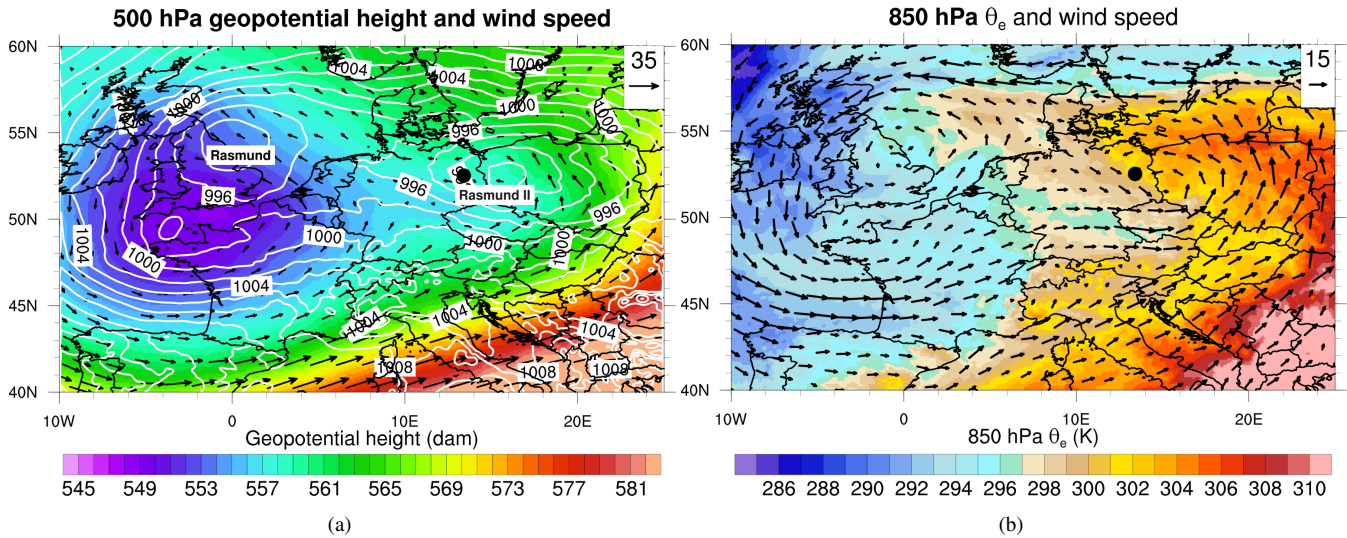


Figure 3. Mean-Sea-Level-a) 500 hPa geopotential height (dam; colour) and wind speed (m s^{-1}) together with sea level pressure (PMSLhPa; contours) and relative topography between 1000 b) 850 hPa and 500 hPa in dam equivalent potential temperature (colour shading θ_e) and wind speed on 29 June, 2017 12 UTC from the ECMWF analysis. The black dot denotes the city of Berlin.

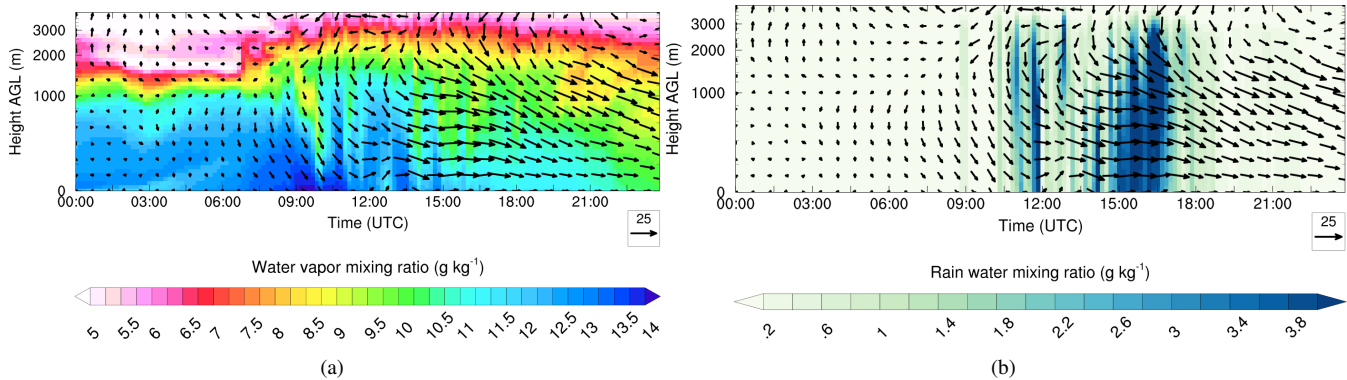


Figure 4. Time-height cross section of (a) water vapour mixing ratio (g kg^{-1}) and (b) rain water mixing ratio (g kg^{-1}) at grid point 13.2°E and 52.85°N (close to the maximum heavy precipitation location, near black dot in Fig. 3) simulated by the WRF model. The displayed period is 00 UTC until 23:45 UTC on 29 June 2017. Arrows denote the horizontal wind speed (m s^{-1} , see lower right of the plots for a length indicating 25 m s^{-1}) and direction at the different altitudes. Altitude is above ground level (AGL).

flow-around-Germany turning into a southerly direction over Poland and eastern Germany with wind speeds of 10 m s^{-1} at 500 hPa (black arrows; Fig. ??a). Weak winds of less than 5 m s^{-1} also occur at 850 hPa (Fig. ??b). 3a) brought a warm and moist cyclonic inflow, crucial for the development of heavy precipitation over Berlin. The Equivalent Potential Temperature (θ_e) at 850 hPa (Fig. ??b) shows 3b) showed values up to 305 K between the Mediterranean and central Europe, from

455 ~~the Mediterranean up to Poland and the Berlin metropolitan area. This is Berlin,~~ indicative of a high moisture availability and optimal conditions for associated stationary deep-moist convection. ~~During daytime (not shown), the strong low-level mid-day convergence together with integrated water vapour values of more than 40 mm led to extreme precipitation in the area. The strong low-level convergence was fostered by the counter circulations of Rasmund and Rasmund II. The low-level wind convergence, crucial for dynamic triggering, took place under the presence of moderate Mixed-Layer CAPE (ML-CAPE)~~
460 ~~of Convective Available Potential Energy (ML-CAPE) at the site was moderate, of approx. 250 J kg⁻¹ and no with Convective Inhibition (CIN). This was was to zero, as shown by the radio sounding deployed in Lindenberg, near Berlin, Lindenberg station (black dot in 3) at 06 UTC 29 June 2017 (see Fig. S2) 2017.~~

The triggering mechanism was a low-level convergence line fostered by the counter circulations of Rasmund and Rasmund II over eastern Germany (Fig. 3), (Gebauer et al., 2017). The encountering circulations also imposed a weak southerly flow atop
465 with 10 m s⁻¹ at 500 hPa (not shown) and less than 5 m s⁻¹ at 850 hPa (black arrows in Fig. 3b). The weak mid-tropospheric flow was responsible for the slow displacement of the convective systems.

a) 500 hPa geopotential height (dam; colour) and wind speed (m s⁻¹) together with sea level pressure (hPa; contours) and b) 850 hPa equivalent potential temperature (θ_e) and wind speed on 29 June, 2017 06 UTC from the ECMWF analysis. The black dot denotes the city of Berlin.

470 ~~The diurnal development of low-level moisture was additionally investigated by means of a high-resolution WRF simulation~~
Values of Precipitable Water Vapour (PWV) up to 40 mm were measured at the Lindenberg station, near Berlin (Fig. S1) at 11:30 UTC, and it is probable that water vapour mixing ratios of more than 6.5 g kg⁻¹ were present at 2500 m above ground level over Berlin 3 h prior to precipitation initiation. This was shown by WRF 1.5 km simulations (Sect. 2.3.1). Fig. 4 shows the time-height cross-section of water vapour mixing ratio (a) and rain water mixing ratio (b), for a covering the greater Berlin
475 area (Fig. 1). For a selected grid point located northwest of the city of Berlin (black dot in Fig. ??), where the largest severe precipitation occurred. The WRF model simulates high 3.a) WRF simulates water vapour mixing ratios of more than 13 g kg⁻¹ in the lowest 100 m above ground between 10 UTC and 19 UTC together with a strong low- to mid-level jet evolving after 13 UTC (Fig. 4a). This low-level jet is probably induced by the temperature gradient between the colder and drier air masses in southwest Germany and the warm and moist air masses over northeastern Germany (Fig. ??a, Fig. S1). ~~These factors led~~
480 ~~to a stronger pressure gradient and thus higher wind speeds. The precipitable water content over the period of interest varies between 40 mm and 44 mm, which is in accordance with the values derived from the Lindenberg sounding (Fig. S2). The 3b).~~
The simulated rain water mixing ratios are very high, exceeding exceeded 3.5 g kg⁻¹ (Fig. 4b), potentially indicating a warm-rain type precipitation event (e.g. Song and Sohn, 2018) which is associated with a strong downdraft of ~ 5 m s⁻¹ (Fig. S3 of the supplementary material S2).

485 Time-height cross-section of (a) water vapour mixing ratio (g kg⁻¹) and (b) rain water mixing ratio (g kg⁻¹) at grid point 13.2 °E and 52.85 °N (close to the maximum heavy precipitation location, near black dot in Fig. ??) simulated by the WRF model. The displayed period is 00 UTC until 23:45 UTC on 29 June 2017. Arrows denote the horizontal wind speed (m s⁻¹, see lower right of the plots for a length indicating 25 m s⁻¹) and direction at the different altitudes. Altitude is above ground level (AGL).

490 4.2 Lagrangian moisture source analysis

To analyse the origin of the atmospheric moisture that led to the large precipitation amounts during the event, we calculate Lagrangian backward trajectories following Sodemann et al. (2008). We calculate trajectories based on ERA5 reanalysis data (Hersbach et al., 2020), in a mid-European region around the center of maximum precipitation (red box in Fig. 9). We start the trajectories from 1000 hPa to 200 hPa in steps of 50 hPa for every hour of 29 June 2017, with a horizontal grid spacing 80 km and going back 240 h in time. From all trajectories, we selected those that have a relative humidity of at least 80 % in the target box and for which the specific humidity decreases during the last time step (precipitation) (Sodemann et al., 2008; Grams et al., 2014). Along each selected trajectory (4,080 out of 15,074 in total), moisture uptake has been computed based on hourly specific humidity increases in the planetary boundary layer associated with evapotranspiration from the surface. The boundary layer height is available as a diagnostic model variable in the ERA5 data set and, again following Sodemann et al. (2008), is multiplied by a factor of 1.5 to account for potential uncertainties in this diagnostic estimate. These uptakes have been weighted according to their contribution to the precipitation (moisture loss) at the target location, taking into account that earlier moisture uptake may contribute less due to precipitation loss on their way to the target region. With this approach, about 49.8 % of the precipitating moisture for the day of 29 June can be traced back to its moisture source.

4.2 Observed lightning activity and accumulated precipitation

To better understand the temporal evolution of the convective development, the spatial distribution of lightning strikes in northeastern Germany is presented (Fig. 4.2a). The combination of low-level wind convergence associated with the surface lows and the warm and moist air masses transported into the region (Fig. ??) favoured thunderstorm Thunderstorm activity in the border region between northeastern Germany and Poland. Already was already active in the morning hours starting at 5 UTC, an initial shaping up a convective line moving westward from Poland towards the city of Berlin produced, producing the first cloud-to-ground lightning along the border (Fig. 4.2a). The system strengthened and hit Berlin mainly between 9 and 10 UTC. Afterwards, the system weakened and moved only slightly further west due to weak upper-level flow. It The convective line remained relatively stationary over the greater Berlin area and west of it until noon (Fig. 4.2a). Upstream of the system, a second thunderstorm line followed, crossing the border between Poland and Germany between 14 and 15 UTC. In the late afternoon, the direction of the convective cells changed and they were transported northward with the weak upper-level flow. In the evening of 29 June 2017, affecting Mecklenburg-Western Pomerania was particularly affected, as well as and the Baltic Sea after 18 UTC.

(a) Cloud-to-ground strokes from the EUCLID data set, colour-coded according to the time of occurrence from 5 UTC on 29 June 2017 to 0 UTC on the following day and (b) 24-hour precipitation totals (mm) during the study period (29 June 2017 06 UTC to 30 June 2017 06 UTC) from REGNIE.

Due to a Due to the weak upper-level flow (Fig. ??3a), the thunderstorms were associated with low propagation speeds leading to high local rain rates. Figure 4.2b shows daily precipitation totals with values up to 200 mm. The convectively enhanced precipitation totals fell mainly in the course of 12 hours in the German states of Brandenburg (BB), Berlin (BE), and south-

ern Mecklenburg-Western Pommern (MV). Very high values above 100 mm were recorded in and northwest of the city of Berlin as well as in an area between Ludwigslust (MV) and Perleberg (BB). For example, Berlin-Tegel (BE) recorded 24-hour precipitation of 196.9 mm, while Zeesen (BB) registered 149.9 mm (Fig. 4.2b and Table S1-S11 in the supplementary material). In many places, more precipitation was measured within 24 hours than the climatological mean for the whole month of June (Wandel, 2017). ~~In the following, we assess the impact that this extreme atmospheric situation had on infrastructure and private households.~~

4.2 Impacts during the 29 June 2017 case

The ~~extreme precipitation event on~~ unusual precipitation totals made the 29 June 2017 HPE one of the most extreme event in the climatology of the greater Berlin area. Based on the PSI method (Sect. 3.1; Caldas-Alvarez et al., 2021; Piper et al., 2016), the 29 June 2017 event around Berlin was the 29th most severe event in the 1951-2021 period (Fig. 6). This event showed a PSI value (1.71), well above the 99th-percentile of the climatology indicating an extreme event. The PSI quantifies the severity of an event considering grid-point precipitation intensity, surface of affected area and persistence. The 29 June 2017 HPE showed a PSI value 2.3 and 30-1.8 times larger than the 29 June 2005 event in Hersbruck and Lohmar (Tab. 1; number 2 in Fig. 6) and the 29 July 2014 event in Muenster and Greven (Tab. 1; number 6 in Fig. 6), respectively. The 26 August 2010 event in Osnabrueck (Tab. 1; number 5 in Fig. 6) is the only event of those assessed in the household surveys with a similar meteorological severity and a similar extent of the damages (€90 Mill.) caused. Compared to other events, the 2002 event in Saxony (number 1 in Fig. 6) showed the most similar meteorological severity. The Ahr flooding in July-2021 (number 9 in Fig. 6) had a PSI value 2.1 lower than the 29 June 2017 ~~heavily impacted the metropolitan area Berlin-Brandenburg (~4.5 HPE due to the weaker grid point intensity (131 Mio. inhabitants)). In total, the event caused €60mm compared to 196.9 Mio. in insured property loss (in 2019 prices)mm~~ and, especially, to the lack of observations over affected areas in Belgium and the Netherlands in REGNIE.

The convective activity and number of cells triggered were also top-ranked compared to other historical cases. Implementing a lagrangian cell tracking algorithm (Sect. 3.2) using 5 min, 1 km radar data (YW RADKLIM), for the period 2001 to 2020, we found that the only event with more cells triggered than the 29 June 2017 HPE was the Saxony 12 August 2002 event (Kreibich et al., 2007). Also outstanding with regard to the number of convective cells triggered were the events on 21 June 2007, ~~most of which occurred in Berlin 22 July 2007 and Brandenburg (GDV, 2018). This makes it the 12 July 2018, where flooding was reported for northern Bavaria, west and south-west Germany and Berlin, respectively (e.g., Kaiser et al., 2021). The former two events showed a strong meteorological severity, with a PSI in the 99th-percentile of the climatology and the latter showed a moderate severity with a PSI close to 0.6.~~ Figure 7 also shows the inverse relationship between the length of the tracks and their number, i.e., the larger the number of cells triggered, the shorter their mean length.

Impacts and monetary losses

Insured losses in the Berlin-Brandenburg area amounted to €60 Mio. (GDV, 2018) making the 29 June 2017 HPE the most damaging extreme ~~precipitation~~ event in Berlin and ~~the Oberhavel district, Brandenburg, Brandenburg~~ in the period 2002-2017 ~~;~~ for which insurance data provide coverage. Insurance data of the GDV ~~show~~ showed that 1.8 % of the buildings in Berlin

incurred damages during the event, with an average loss of €6,830. The Oberhavel district was more heavily affected, with 5.3 % of the buildings damaged and an average loss of €10,550 (GDV, 2021). In Berlin, the long-lasting rainfall overloaded the sewer system, resulting in widespread inundation that caused disruption of traffic (i.e., blocked roads), flooded basements and underground stations, as well as intangible consequences including restrictions in daily routine and mental discomfort (GDV, 2018; Berghäuser et al., 2021). The high number of rainfall-related missions on these two days forced the Berlin fire brigade to declare an ‘exceptional weather situation status’ (Kox and Lüder, 2021). The small municipality of Leegebruch (~6,800 inhabitants, located 40 km north of Berlin in the Oberhavel district) was even more severely affected due to its location in a topographical depression and a typically high groundwater table. The resulting inundation cut off the settlement from its surroundings, affected 40 % of the municipality, and persisted for several weeks (GDV, 2018).

Table 1. Pluvial flooding events where surveys were conducted at affected households. Five events were surveyed at seven locations. The start and end dates, the affected area, the maximum daily precipitation, and the affected population are obtained from the CatRaRe database (Sec. ??2), based on RADKLIM precipitation data. The overall losses within the municipality (*) are from GDV (2020) and refer to insured losses, while loss values with a (**) are from Hydrotec et al. (2008) and refer to total losses (non-insured and insured losses). Losses are referred to constant 2019 prices. Note that Hersbruck was hit by two events in close succession, which are listed separately.

City	Date Start yyyy-mm-dd	Date End yyyy-mm-dd	Aff. Area km ²	Max. Prec. mm	Population 10 ³ people	Losses Mio. €	Surveys
Berlin	2017-06-29 10:50	2017-06-30 10:50	31,661.4	161.9	6,529	60 (*)	28
Leegebruch	2017-06-29 10:50	2017-06-30 10:50					88
Muenster	2014-07-28 13:50	2014-07-28 22:50	1,117.3	175.8	594	330 (*)	447
Greven	2014-07-28 13:50	2014-07-28 22:50					63
Osnabrueck	2010-08-26 04:50	2010-08-27 04:50	13,426.9	163.9	4,975	90 (*)	100
Hersbruck	2005-06-29 05:50	2005-06-29 07:50	53.6	42.8	20	4 (**)	111
Hersbruck	2005-06-29 20:50	2005-06-29 22:50		39.8	19		
Lohmar	2005-06-29 00:50	2005-06-30 00:50	2,669.7	100.9	2,571	3.5 (**)	62

Table 1 compares the meteorological severity, the impacts and the number of surveyed households between the [Berlin-Leegebruch-2017 29 June 2017 HPE in Berlin and Leegebruch](#) event and the events in Muenster and Greven (~~impacted in~~-2014), Osnabrueck (~~impacted in~~-2010) and Hersbruck and Lohmar (~~both impacted in~~-2005). The meteorological indicators (~~derived from CatRaRe~~) show that the Berlin-Leegebruch-2017 event was characterised by its large spatial extent (~~31,661 km²~~) and long rainfall duration (~~approx. 24 hours~~). As shown in Sect. ??4.1, the long rainfall duration was caused by the slow propagation of the convective system given the weak mid-tropospheric winds. The maximum accumulated precipitation in Berlin, ~~shown in~~ (Table 1), somewhat differs from the REGNIE observations (Fig. 4.2b) since the values of CatRaRe are based on the RAD-KLIM RW 1-hour product that uses a different gridding method and data source. ~~The other events affected considerably smaller areas and, in the case of Muenster-Greven-2014 and Hersbruck-2005, persisted for a shorter period. The maximum precipitation depth in Berlin-Leegebruch-2017 was exceeded by the events in Muenster-Greven-2014 and Osnabrueck-2010. The aggregated~~

event loss in Berlin-Leegebruch-2017 was lower than the losses caused by the extreme rainfalls in Muenster-Greven-2014 and Osnabrueck-2010, although the Berlin-Leegebruch-2017 event affected the largest number of people. The events in Hersbruck-2005 and Lohmar-2005 exhibited less intense rainfall and substantially smaller losses.

Figure 8 allows for a more detailed view of the impacts and related mechanisms by looking at the distributions of surveyed flood indicators and monetary losses at a household level. The ~~figure panels show the distributions of the inundation depth in the basement, the inundation duration and the building losses that were reported by private households affected by the respective pluvial flood events. The highest basement inundation depths occurred in Muenster-2014 and Hersbruck-2005. In Leegebruch-2017 and Berlin-2017, results reveal that~~ basements were inundated less severely in Leegebruch-2017 and Berlin-2017 than in the other events. ~~The Further, the~~ inundation durations in Berlin-2017 (median of 72 hours) and Leegebruch-2017 (median: 92 hours) exceed the inundation durations of the other events ~~considerably, which do not exceed 24 hours (Fig. 8b; note the log-scale)~~. Monetary losses to buildings were particularly large in Leegebruch-2017, Muenster-2014 and Osnabrueck-2010, where approximately 75 % of the surveyed households reported a loss of ~~€1000~~ €1,000 and more. In addition, ~~building loss exceeded €9,999 in more than 25 % of the cases and the largest loss category is relatively abundant. In~~ Leegebruch-2017, almost half of the surveyed households suffered building loss in the largest two categories (\geq €10,000).

~~In summary, the Berlin-Brandenburg-2017 was very extreme with respect to precipitation and flood duration, large spatial extent and extraordinary monetary losses. The joint evaluation of the CatRaRE and survey data reveals no uniform~~ Altogether, a clear relationship between precipitation indices (intensity, duration, extent) and resulting losses across the group of study cases. ~~In contrast could not be found. Instead,~~ flood characteristics at the affected buildings (inundation depth and duration) can explain much (although not all) of the incurred losses. Ultimately, flooding in urban areas is a complex process that depends not only on the meteorological nature of an event but also on the local characteristics of the terrain defined by topography, land use, sewer system capacity and operability, and hydro-geology, as well as on socioeconomic conditions such as settlement structure, building codes and private risk-mitigation.

4.2 Lagrangian moisture trajectories

4.3 **Probability of exceedance and severity**

~~In this section we quantify the return periods and severity for this event. A sufficiently moist environment is needed for deep moist convection to develop (Markowski and Richardson, 2010). Section 4.1 showed how a very moist atmosphere with up to 40 mm of Precipitable Water Vapour preconditioned the initiation of convection in the greater Berlin area. Now the question is where did the precipitating moisture originate. To this end we use Lagrangian backward trajectories based on hourly ERA-5 data (Sect. 4.2).~~

605 4.2.1 **Probability of exceedance (return periods)**

~~We estimate return periods using the Gumbel distribution (Eq. 2)~~ We found that land masses were the main sources of moisture uptake. Out of the selected 15, the GEV distribution (Eq. 074 trajectories fulfilling the selection criteria, 82.9 % originated over

land areas, whereas only 17.1% of the precipitating moisture evaporated over the ocean. With this method, about 49.8% of the precipitating moisture for the day of 29 June could be traced back to its moisture source. The eastern European region (around 10°E to 32°E and 37°N to 60°N) was by far the main source of moisture uptake (63.0%). Additionally, the moisture uptake in this region was relatively evenly distributed, ranging from Poland (east of the precipitation event) towards Croatia and Italy, with a maximum moisture uptake of about 4.6 mm per single grid point (Fig. 1) applied to spatially averaged data and a duration-dependent GEV (Eq. 9). Other, but less important, land moisture sources were the western European region (around 12°W to 10°E and 37°N to 60°N), with a contribution of 13.9%; see Sect. 3, and the northern African region (around 20°W to 32°E and 20°N to 37°N), with a contribution of 5.9%. The oceanic moisture sources were primarily the Mediterranean Sea (11.9%) and Atlantic Ocean (4.6%), but these played a minor role compared to the moisture uptake over land. A similarly important role of moisture recycling from land sources has been found previously for an extreme precipitation event in eastern Europe in May 2010 (Winschall et al., 2014) and for the central European floods in June 2013 (Grams et al., 2014; Kelemen et al., 2016). In the case of the 29 June 2017 HPE studied here, moisture recycling likely happened on relatively short time scales of 1-2 days, as June 2017 was generally dry, but northeastern Italy, Slovenia, Austria and southeastern Poland were affected by convective precipitation on 28 June. The moistening of the soil due to prior precipitation is thus hypothesised to be an important precondition for the Berlin event. While each approach has benefits and shortcomings (e. g. available data set, computing time), they all show that the event analysed was a rare event.

The

625 4.3 GEV models and return periods

We provide an estimation on how rare the 29 June 2017 HPE was calculating probabilities of exceedance p and return periods t_{RP} fitting observations of extreme precipitation to GEV models (Sect. 3.5). Return values RV_{RP} (quantiles) and the associated return periods t_{RP} , or directly the probability of exceedances p , are related to the GEV distribution as $t_{RP} = 1/(1 - G(RV_{RP}))$ (Coles, 2001). For example, a probability of exceedance $p = 0.01$ for annual data can be interpreted as on average 1 event in 100 years rare an event has been. This information is also used by reinsurance companies and hydrological studies.

We start by estimating return periods using the Gumbel distribution (Eq. 2) is used to estimate exceedance probabilities and associated return periods per grid-point ($1 \times 1 \text{ km}^2$) for 24-hour precipitation totals in Germany based on a 70 year time series (REGNIE; Fig. 10). The results show return periods of more than 200 years between Ludwigslust (MV), Perleberg (BB) and Berlin; covering a total area of 8.729 km^2 . Past work has shown how estimated return periods that are much longer than the observational record exhibit large uncertainty (Makkonen, 2006; Grieser et al., 2007). This is why we truncate all return periods above 200 years (Fig. 10), acknowledging that the 70 year observational record might be too short to provide accurate values for such long return periods.

The second approach, consisting of fitting a GEV distribution to spatial averages of different size also showed very large return periods, however decreasing with increasing size of the considered areas. The rationale behind this analysis is that return periods at individual grid points may not best-characterise the event and its associated impacts since an event with a very long return period at a given site can have a small spatial extent. Such a situation will lead to less flooding than an event with

~~similar precipitation intensities which is spatially larger. Such~~ spatial averaging of observations is also required for validation of simulated return periods in climate models and assessment of the model biases (see e.g. Philip et al., 2020).

For this approach we fit a standard GEV distribution (Eq. 1) and estimate return periods of the yearly block maxima of REGNIE precipitation data from 1951 to 2020, spatially averaged over three boxes of different size (brown, grey, and pink boxes in Fig. 10 and Table S2-S2 in the supplementary material). The results show that the return period of the event decreases with increasing box size. At the finest analysed scale (340 km^2 ; pink polygon in Fig. 10), the extreme event has a return period of over 420 years, which decreases to 75 years for the largest area ($11,100 \text{ km}^2$; brown polygon ~~) due to the regional scale of this extreme event~~ in Fig. 10). Compared to other historical events, the precipitation of 29 June 2017 HPE was the most extreme ~~observed event~~ in the time series when considering the smallest analysed region, however, an event with a larger spatially-averaged precipitation sum and thus a larger return period was detected on 8 August 1978 in the two larger areas (grey and brown boxes). In the supplementary material, the return period of the 29 June 2017 event HPE is compared to the July 2021 heavy rainfall event impacting Western Europe.

One useful approach to reduce uncertainty in the estimation of return periods from temporally short observational records is using different accumulation durations between 1 hour and 3 days (Eq. 3), however at the expense of more demanding computing power. The d -GEV model (Eq. 3) is applied to grid point intensity from RADKLIM RW (2001 – 2020; Fig. 11a). For this dataset, the estimated d -GEV shape parameter ξ has a median value of 0.24. Accumulations (duration d) of one day showed very high return periods (> 800 years) for seven grid points in north-western Berlin. Over this area, most grid points showed return periods between 50 and 200 years. The small grid box size of $1 \text{ km} \times 1 \text{ km}$ could explain the very high return periods in cases of statistical outliers. On shorter time scales of 8 hours and 1 hour, north-western Berlin shows lower return periods, between 10 and 100 years for the two former temporal aggregations and between 2 and 10 for the latter (Fig. 11.a). The short time range of historical RADKLIM data (20 years), however, limits the reliability of these spatially resolved return period estimates.

To overcome the short time span of the RADKLIM dataset, we implement a duration-dependent GEV model (Eq. 3) on DWD ground station data at Berlin-Tempelhof (Fig. 1). The return levels (quantiles) for any exceedance probability and time scale (duration d) are presented in Intensity-Duration-Frequency (IDF) curves (Fig. 11). This station was chosen because data records are longer than the RADKLIM data. 10-minute aggregations span 1995 to 2020 and daily aggregations cover the period 1948 to 2020. The longer time series lead to shorter and—due to the reduced uncertainty—potentially more plausible return periods. The analysis shows return periods of 100 years for durations above than 10 hours, 114 years for daily aggregations. However, confidence intervals in the IDF curves also remain large (Fig. 11b).

All used approaches highlight that the analysed event was rare, with return periods longer than 100 years in the Berlin area. The efficient use of information from the observation data (accumulation periods from 10 minutes to 3 days) lead to more plausible return period estimation from the d -GEV model, compared to Gumbel using daily accumulations. However, long data records with high measurement frequency and enough computing resources are not always available, in which case a non-duration-dependent model using daily data could be a better choice. Finally, including a climate change signal into the

d-GEV estimation (Ganguli and Coulibaly, 2017) could improve the results, since the assumption of a non-changing climate leads to over-estimated return periods for events that become more likely with climate change.

4.3.1 Severity

In addition to the estimation of return periods, we assess how extreme the 29 June 2017 event was in terms of severity. We use the Precipitation Severity Index (PSI; Caldas-Alvarez et al., 2022) to detect extreme precipitation events according to three different but complementary characteristics of heavy precipitation: intensity, spatial extent and persistence. The PSI in its current form is an adaptation of the Storm Severity Index (SSI; Leekebusch et al., 2008; Pinto et al., 2012) and is a unitless index that indicates the degree of daily precipitation severity with respect to a predetermined climatological threshold (in our case the 80th percentile). Large PSI values represent high intensity, geographically extensive and temporally persistent precipitation events.

Temporal evolution of the PSI (blue bars). The results are based on REGNIE daily precipitation observations between January 1951 and September 2021. The 99-percentile and 90-percentile of daily PSI values are represented by the dashed blue horizontal lines. Numbered circles highlight nine events analysed in Table 1 or in Fig. 7 as well as other historical events. These are (1) the Saxony floodings on the 12 August 2002; (2) the 29 June 2005 event, affecting Hersbruch and Lohmar; (3) the 21 June 2007 and the (4) 22 July 2007 events affecting Germany in its totality; (5) the 26 August 2010 event in Osnabrueck; (6) the 29 July 2014 event in Muenster and Greven; (7) the 29 June 2017 event (red); (8) the 12 July 2018 causing flooding in Berlin; and (9) the Ahr flooding on 14 July 2021.

Figure 6 shows the temporal evolution of daily PSI values between January 1951 and September 2021 from daily REGNIE observations. The PSI values of 9 historical events from Tab. 1 and Fig. 7 are shown. The PSI analysis shows that, in terms of meteorological severity, the 29 June 2017 event around Berlin was the 29th most severe event in the 1951-2021 period, well above the 99th percentile of the climatology (Fig6). The severity of the 29 June 2017 case was found to be 2.3 and 1.8 times larger than the 29 June 2005 event in Hersbruch and Lohmar (Tab. 1; number 2 in Fig. 6) and the 29 July 2014 event in Muenster and Greven (Tab. 1; number 6 in Tab. 1), respectively. The 26 August 2010 event in Osnabrueck (Tab. 1; number 5 in Fig. 6) is the only event of those assessed in the household surveys with a similar meteorological severity and a similar extent of the caused damages (€90 Mio.; Tab. 1). Compared to other events, the 2002 event in Saxony causing large flooding (number 1 in Fig. 6) showed the most similar meteorological severity. The Ahr flooding in July 2021 (number 7 in Fig. 6) had a PSI value 2.1 lower than the 29 June 2017 event due to the weaker grid point intensity (131 mm compared to 196.9 mm) and, especially, to the lack observations over affected areas in Belgium and the Netherlands in REGNIE.

To further classify the severity of the 29 June 2017 in the climatology we implement a simple cell tracking algorithm, originally developed for isolated convection (Steinacker et al., 2000; Purr et al., 2021) on 5 min, 1 km radar (YW-RADKLIM), for the period 2001 to 2020 over Germany.

Figure 7 shows a scatter plot of events in that period where the number of detected tracks is compared to their mean length. Events are divided into two groups, depending on whether a prevailing wind direction and cyclonic circulation was present (red) or not (blue). The only event with more cells triggered than 29 June 2017 is the 12 August 2002 event, which caused the

710 historical floods in Saxony (Kreibich et al., 2007). Also outstanding with regard to the number of convective cells triggered
were the events on 21 June 2007, 22 July 2007 and 12 July 2018, where flooding was reported for northern Bavaria, west and
south-west Germany and Berlin, respectively (e.g., Kaiser et al., 2021). The former two events showed a strong meteorological
severity, with a PSI in the 99th-percentile of the climatology and the latter showed a moderate severity with a PSI close to 0.6.
715 Figure 7 also shows the inverse relationship between the length of the tracks and their number, i.e., the larger the number of
cells triggered, the shorter their mean length. Moreover, Fig. 7 shows that a large number of extreme events in the 2001 to 2020
period belong to the XXCCW weather type (Bissolli and Dittmann, 2001).

Cell track characteristics (mean length and number of tracks) for the research area Berlin and surroundings for days from
2001 to 2020. Colour coding identifies if days have been classified as weather type ‘no prevailing wind direction, cyclonic
circulation in 950 and 500 hPa and above-average humidity content of the troposphere – XXCCW’ or another type (not
720 XXCCW). Arrows indicate days with flooding events in Germany.

4.4 **Extreme Conditional event attribution**

A full understanding of an observed extreme event requires addressing the question of how the event relates to anthropogenic
influences. This is particularly important with respect to climate-change communication with stakeholders and the general
public. The field of extreme event attribution seeks to address such questions by examining whether, and to what extent,
725 anthropogenic influences may have affected the severity and/or frequency of a specific extreme.

4.4.1 **Conditional event attribution**

For conditional attribution, the modelling approach involves simulating an event under present-climate conditions and then re-
peating the simulation with modified boundary conditions. This modification consists of subtracting the vertical thermodynamical
climate-change signal (Lackmann, 2015; Pall et al., 2017) and is, thus, particularly amenable to high-resolution (convection-
730 permitting) regional-model experiments, which have many advantages for modelling extreme precipitation (Meredith et al.,
2020, 2021; Stevens et al., 2020). The modelling approach is, in essence, an adaptation of the surrogate global-warming
method (Schär et al., 1996; Hibino et al., 2018; Kröner et al., 2017). The results presented here are based on the model simu-
lations described in Section 3.6. Analysis, where the analysis is performed over an area of 81,520 km² centred on the event
location (Fig. S3). Model evaluation and technical details are found in the Supplementary Material.

735 (a) Vertical warming signal and (b) response of event precipitation to warming signal. The warming is based on a subset of
17 CMIP6 models. The x-axis in (b) shows precipitation bins which are delineated by quantiles of the precipitation intensity
distribution; the changes in area and volume represent the changes associated with precipitation in these bins. Based on the
Wilcoxon-Mann-Whitney test, the total changes given within (b) are all statistically significant with at least $p < 0.02$. Shading
denotes the 95% confidence intervals based on 1,000 bootstrap resamples.

740 The thermodynamical climate-change signal is vertically heterogeneous, with stronger warming in the mid and upper tropo-
sphere (Fig. 12a). Based on a mean tropospheric (1,000 – 300 hPa) temperature of ~ 269 K and warming of 1.36 K, this implies

an increase in saturation vapour pressure of $\sim 10.5\%$ (Bolton, 1980), which exceeds the 7.5 % increase in precipitable water we find (7.5 %, (time average; not shown) -which we find over our eastern-Germany analysis region (Fig. S3).

In our present-climate simulations, we find a low, though statistically significant ($p < 0.02$), increase in total precipitation volume of 4 %. This can be better understood by analysing both changes in the precipitation distribution and physical characteristics of the convective system (Fig. 12b). Changes in total precipitation volume associated with a given quantile of precipitation intensity increase as the quantiles become higher. Indeed, at the lowest intensity quantiles, the associated precipitation volumes are found to decrease, which partly offsets the volume increases associated with the higher intensity quantiles (Fig. 12b). By breaking the total precipitation volume into its area and depth components, it can be seen that the change in precipitation intensity shows a signal very similar to that of the total precipitation volume. The spatial extent of the precipitation, meanwhile, decreases (-2 %) in the warmer climate, in line with the results of Wasko et al. (2016) and Armon et al. (2022). It is thus clear that it is not changes in the spatial extent of the system, but rather higher local intensities which drive the increase in total precipitation volume. The intensities increase for, approximately, the upper half of the precipitation distribution, peaking at a 10.4 % increase for the highest quantiles. This increase exceeds the increase in precipitable water (see above), implying that local moisture convergence was an important factor for the most extreme intensities.

It is worth noting that, based on the average tropospheric warming signal (see above), the intensification of the highest quantiles corresponds (almost exactly) to what would be expected from the Clausius-Clapeyron relation. Had the precipitation-temperature scaling been computed using the lower troposphere or the 2-m temperature instead, a super Clausius-Clapeyron increase would have been found. Currently, it is still a matter of debate as to which temperature is most appropriate to use when computing the scaling rate (Drobinski et al., 2016; Formayer and Fritz, 2017). It is plausible that the total precipitation would not have shown an attributable change but that the most intense quantiles would have. This insight is also of relevance for impact studies: the effect of climate change was found to be dependent on the spatial scale of interest. We conclude by stating that climate change since the pre-industrial era served to increase the magnitude and, in particular, the highest precipitation intensities of the event.

765 **4.4.1 Role of Aerosols**

4.5 Sensitivity to aerosol loading

Another influence of anthropogenic activities, transport, industry, etc. on heavy precipitation is via cloud-active aerosols. Aerosols may affect deep convection in various ways (Rosenfeld et al., 2014; Fan et al., 2015) and thus exert an anthropogenic effect beyond the impact of global warming. For instance, an increased aerosol number reduces droplet size by increasing the condensation nucleae and the droplet concentration leading to enhanced precipitation (Guo et al., 2022).

~~The~~

We study the role of cloud-active aerosol within the aerosols within the 29 June 2017 event was examined using simulations HPE through sensitivity experiments with the ICON model shown in Fig. 13 (see Sect. ?? at 625 m resolution, comparing two scenarios (Sect. 3.7). The first one has factual concentrations representative of the 29 June 2017 HPE, which is a comparatively

775 ~~clean situation (CLN). The second one, has aerosol concentrations representative of the peak-aerosol conditions in the mid-1980s, or polluted scenario (POL). The simulated distribution of precipitation is compared with RADKLIM for the period from 06 UTC 29 June 2017 to 06 UTC 30 June 2017 (Fig. 13). In order to assess the importance of aerosols for this extreme event, two simulations are performed with different aerosol number concentrations. The first one has factual concentrations representative of the 2017 event, which is a comparatively clean situation (CLN). The second one, has aerosol concentrations representative~~
780 ~~of the peak-aerosol conditions in the mid-1980s, or polluted scenario (POL). The.~~

The results show that POL simulates an increase in increased cloud number and cloud mass due to the increased larger aerosol loading (not shown). This is particularly seen in the heavy precipitation with the corresponding heavy precipitation increase. This is especially so for intensities exceeding 150 mm d⁻¹ (Fig. 13c). These would have been higher by We quantified this increase in probability to be of 70 % in the high-aerosol conditions as in the 1980s (compared to the factual case (CLN) during the 29 June 2017 HPE. In POL 4.3 % of grid points exceeded exceeded 150 mm 24 d⁻¹ in the high-aerosol case compared to 2.3 % in the low-aerosol simulation). (CLN).

785

5 Conclusions and outlook

~~HPEs Multi-disciplinary analyses are a powerful means to gain full understanding of heavy precipitation events with high impact are gaining attention in the scientific community and the general public. Events such as the one assessed here, affecting~~
790 ~~the Berlin metropolitan area in June 2017, or the Ahr event in western Germany in July Ahr flooding events in northern Europe in 2021 (Kreienkamp et al., 2021) are evidence of the tremendous damaging potential of this atmospheric phenomenon. Multidisciplinary studies, combining expertise from different research fields are a powerful means to provide novel information about interconnected aspects of extreme precipitation. Here we used the synergy of the project ClimXtreme to combine different methods for (Kreienkamp et al., 2021; Mohr et al., 2022). In this work we implemented analytical methods from~~
795 ~~impact, meteorological, and climate sciences using state-of-art observational and modelling data sets to provide a comprehensive assessment of a selected case study, the 29 June 2017 HPE in the metropolitan area of Berlin (Germany), from the meteorological, impacts and climate perspectives, additionally estimating the contribution of climate change to its extremeness. The main conclusions of the study are:.~~

The The 29 June 2017 event occurred under the influence of a mid-tropospheric trough over western Europe (TrW pattern),
800 with two principal short-wave surface lows located east of the British Isles (Rasmusd) and over western Poland (Rasmusd II) between 29 and 30 June. Rasmusd II induced a southwesterly flow bringing moist and warm warm and moist air ($\theta_e^{850} = 306$ K, IWV = 42 mm), accompanied by moderate ML-CAPE over the Berlin area(250 J kg⁻¹). Low-level wind convergence along the German-Polish border triggered several thousand convective cells initiated convection, inducing more than 11000 convective cells and lightning, starting 5 UTC (29 June) that displaced displacing northwards slowly due to the weak tropospheric horizon-
805 tal winds (10 m s⁻¹ at 500 hPa). Lagrangian backward trajectories determined that the continental region between Poland and northern Italy was the major moisture source feeding the systems with uptakes up to 4.6 mm. Lightning activity was especially active over this area between 05 UTC and 19 UTC (29 June), displacing towards the (northern) Baltic Sea by 23 UTC. Total

extreme precipitation amounted ~~locally~~ to 196 mm in 24 h, especially impacting the Berlin area and the southern limit of the Mecklenburg-Western Pomerania state.

810 ~~The analysis of the impacts showed that the~~ A climate index, based on precipitation intensity, coverage, and persistence, classified this event as the 29 June 2017 case as the costliest event between 2002 and 2017 in the greater Berlin area, with €60 Mill.th most severe on record since 1951 in Germany.

Total insured losses in properties amounted to €60 Mill. due to widespread inundation, traffic disruptions and basement flooding. This made the 29 June 2017 HPE the costliest event between 2002 and 2017 in the greater Berlin area. A set of
815 unique surveys estimating the losses at the household level allowed us to compare the 2017 HPE in Berlin and Brandenburg with previous historical cases in Hersbruck and Lohmar in 2005, Osnabrueck in 2010 and Muenster in 2014. The 2017 HPE stands out in terms of median inundation duration, which was up to 100 h; 4 to 12 times longer than the other surveyed events. While surveyed flood attributes (inundation depth and duration) can be linked to household losses, it is difficult to establish a link between these attributes and the meteorological characteristics of the event. This is because the impact at the household
820 level is not only caused by the meteorological characteristics, but also by the conditions on the ground.

~~In addition to the impacts perspective, we categorized the event as extreme in terms of frequency of occurrence and severity compared to the climatology. Based on three~~ Lagrangian backward trajectories determined that land masses, instead of water bodies were the main sources of atmospheric moisture feeding the systems, accounting for 82.9 % of the identified precipitating moisture. In particular, the continental region between southern Poland and northern Italy was the major moisture source, with uptakes up to 4.6 mm in 240 h. It is hypotesised that this moisture was recycled from an earlier event, impacting Slovenia, Austria and Poland on the 28 June.

~~Three different~~ approaches using Generalized Extreme Value (GEV) models (Gumbel, standard, and duration-dependent) ; ~~this event showed return periods larger than~~ quantified the return period of this event to be over 100 years for daily precipitation observations, between the greater Berlin area and the southern limit of Mecklenburg-West Pomerania aggregations. For higher
830 temporal resolution observations ~~of this event~~, the return periods were reduced to intervals between 10 to and 100 years and for 8-hour aggregations, and between 1 to and 10 years for aggregations of 8 and 1 hours, respectively 1-hour aggregations. For spatial averages over an area of the scale of the event (11,100 km²), return periods were of 75 years. ~~Furthermore, a precipitation-based index (PSI) classified the~~ 29 June 2017 case as the 29th most severe event in the 1951-2021 climatology. ~~While these techniques provided a good estimation of the probability of exceedence and return periods of such events, our analysis highlighted the large uncertainty of obtaining large return periods~~ This event was further identified as extreme by Lagrangian cell tracking, classifying the 29 June 2017 case as the second event in the period 2001–2020 in terms of number of cells triggered, only behind the historical 2002 flooding in Saxony-70 years in our case). To overcome this problem, we suggested using station data, which is usually available for longer periods, at different
840 temporal resolutions with a duration-dependent GEV model. Thereby we were able to increase the sample size and shrink the confidence intervals. Other interesting approaches to be tested in further research are, considering the climate change signal for *d*-GEV estimation (Ganguli and Coulibaly, 2017), or using spatial models (Ulrich et al., 2020; Berghäuser et al., 2021) that combine information from several stations into one model using spatial covariates.

The attribution experiments for this case study showed that the thermodynamic climate change signal since the pre-industrial era caused a small, but significant increase in heavy precipitation for this event. While total precipitation increased by 4 %, the heaviest precipitation rates showed an intensification of over 10 %. Moreover, ~~aerosol sensitivity experiments showed larger cloud mass and increased probability of extreme precipitation rates (> in addition to the thermodynamical effect of climate change, anthropogenic aerosol emissions could increase the probability of heavy precipitation rates over 150 mm d⁻¹), in a polluted scenario compared to the factual situation for this event as shown by hectometer scale model sensitivity experiments with different aerosol loadings.~~

The combined use of impacts, meteorological and climate methods allowed us to relate diverse aspects of heavy precipitation. We found, for the 29 June 2017 event HPE, that large amounts of moisture from continental evaporative sources added to the slow motion of the convective systems to cause one of the most extreme events to date. Furthermore, we related the meteorological extremeness to the impacts for this case, provided the event's large return periods and severity and the reported losses of up to (€60 Mill.). This relationship, however, should not be understood trivially, since precipitation severity is a necessary but not sufficient condition for high precipitation damages. For the 29 June 2017 event, the state of the ground conditions, i.e. blocking of the sewer system in Berlin and Leegebruch was determinant in inducing the high costs. Finally, the climate attribution experiments demonstrated that a part of the severity of one of the most extreme events of the last 70 years in Germany was attributable to the already-observed changes in the thermodynamical environmental conditions.

Notwithstanding the advantages of multidisciplinary studies, they can suffer from methodological and data inconsistencies; ~~e. g. when data sets show relevant biases.~~ An example of this, is the use of different numerical models. We decided to use different models to profit from the techniques best known to the different working groups. Moreover, we are confident that our results are model independent since all models showed a similar dynamical evolution of the event. Whereas discrepancies in the methods ~~cannot be easily overcome, are to a large extent unavoidable~~ as they are intrinsic to the synergistic approach used in this study, the validation of observations provides a powerful means to reduce uncertainty regarding data biases. Our validation of precipitation data sets in Section 2 showed a high degree of agreement and accuracy between the different products, providing confidence in the conclusions drawn. Among the used products, the accuracy was especially high for REGNIE, followed by RADKLIM.

~~Also worthy of discussion are the advancements made for the calculation of return periods and fitting of GEV models. While these techniques provide a good estimation of how anomalous an HPE is, our analysis also highlights the large uncertainty of estimating very large return periods (>100 years) from temporally short databases (<70 years in our case). To overcome this problem, we used station data, which is usually available for longer periods, at different temporal resolutions with a duration-dependent GEV model. Thereby we were able to increase the sample size and shrink the confidence intervals. Other interesting approaches suggested by previous studies are: considering the climate change signal for *d*-GEV estimation (Ganguli and Coulibaly, 2017), or using spatial models (Ulrich et al., 2020; Berghäuser et al., 2021) that combine information from several stations into one model by using spatial covariates to estimate GEV parameters.~~

Finally, the multidisciplinary collaboration has created powerful connections that will be exploited in up-coming research. For instance, the authors of this paper will form an expert task force in the framework of ClimXtreme to assess future precipitation events of high interest for the media and the general public, such as the Ahr event in 2021, shortly after their occurrence.

Code availability. The WRF model source code can be obtained from <https://github.com/wrf-model/WRF/archive/refs/tags/v4.2.1.tar.gz>.

880 The COSMO-CLM model is accessible to members of the Climate Limited-area Modeling Community, and access is granted upon request. Parts of the model documentation are freely available at <https://doi.org/10.1127/0941-2948/2008/0309> (Rockel et al., 2008)

Data availability. REGNIE, RADKLIM, German precipitation station and CatRaRe data from the DWD used in this paper are freely available for research under the Open Data Portal (DWD, n.d.-a). Lightning EUCLID data are not freely available but can be requested from the Blitz-Informationdienst von Siemens (<https://new.siemens.com/de/de/produkte/services/blids.html>). ERA5 data are available via the Copernicus Climate Change Service (C3S; <https://climate.copernicus.eu/>; last access: 01 January 2022)(Hersbach et al., 2018). ECMWF analysis data can be obtained from <https://apps.ecmwf.int/archive-catalogue/?type=an&class=od&stream=oper&expver=1> (last access: 24 August 2021) (ECMWF, 2021). The user's affiliation needs to belong to an ECMWF member state. The WRF model simulation data can be made available by TS upon request. The COSMO-CLM simulations have been deposited in an open-access repository at the World Data Centre for Climate (WDCC) under the permanent link https://cera-www.dkrz.de/WDCC/ui/cersearch/entry?acronym=DKRZ_LTA_1152_ds000301.

890 The survey data of the Lohmar (2005), Hersbruck (2005) and Osnabrück (2010) events are available via the German flood loss database HOWAS21 at <https://doi.org/10.1594/GFZ.SDDB.HOWAS21> (German Research Centre for Geosciences GFZ, 2022). The data of the Münster (2014) event will be added to HOWAS21 by the end of 2023 and can currently be provided upon request. The Leegebruch (2017) and Berlin (2017) surveys are available upon request. ICON simulations (aerosol attribution) are archived in long-term storage at DKRZ and as redundant copy at Leipzig University, please send data requests to RC.

895 *Author contributions.* All authors collaborated and contributed to drafting, reviewing and editing the paper. In particular, ACA and JQ coordinated the effort and wrote the abstract and conclusions of the manuscript; KB, LD, MH, EPM, SM, JQ, LS, TS and JST wrote the introduction; SS, DN and FK provided support for data management and precipitation dataset validation; AK performed the Lagrangian cyclone analysis; MA, SM, TS and VW analysed the synoptic and mesoscale conditions; FR and SP performed moisture backward trajectory analysis; GA, LD, MH, HK, LS and AHT provided the impact analysis and household surveys; JST, SM and FF implemented the generalized extreme value models and estimated the return periods; HF, EELE and ACA implemented the precipitation severity index; KB implemented the Lagrangian cell tracking algorithm; EPM contributed the conditional event attribution experiment; JQ and RC performed the aerosol sensitivity experiments.

Competing interests. The authors declare that they have no competing interests.

Acknowledgements. This study is the outcome of collaborative work in the "ClimXtreme" project funded by the German Ministry of Education and Research (Bundesministerium für Bildung und Forschung, BMBF) in its strategy "Research for Sustainability" (FONA). The following subprojects have been funded by ClimXtreme. ACA and HF (project SEVERE) and SM and MA (project VarCLuST) sincerely thank the BMBF for funding the two projects (grant number 01LP1901A). TS is funded by the project LAFEP (grant number 01LP1902D); EM is funded by the project XPreCCC (grant number 01LP1902H). RC and JQ gratefully acknowledge PATERA (FKZ 01LP1902C). KB is funded by the project DCUA (grant number 01LP1905A). AK sincerely thanks the project B3.6 LAMCoX (grant number 01LP1902F) for their funding and support. HK acknowledges the project FLOOD (01LP1903E). FR and SP are funded by the project MExRain (grant number 01LP1901C). The contribution regarding IDF curves was sponsored by BMBF and the project IDF-AF (grant number 01LP1902H). JST is funded through the project AXE-G (grant number 01LP1902B). EELE is funded by the project CoSoX (grant number 01LP1904C). GA and LD are funded by the project CARLOFFF (BMBF, grant number 01LP1903B), LS by the DFG (GRK 2043/2). DN and SS are funded by CoDaX (BMBF, grant number 01LP1904A). This work used computing resources of the German Climate Computing Center (DKRZ) granted by its Scientific Steering Committee (WLA) under project IDs bb1152 and bm1159. We thank the CLM-Community (<https://wiki.coast.hereon.de/clmcom>) for maintaining and providing the COSMO-CLM regional climate model. ECMWF is acknowledged for providing the operational IFS analysis data on model levels and for providing the ERA5 data. The ERA5 reanalysis data used in this study contain modified Copernicus Climate Change Service Information 2020. Neither The European Commission nor ECMWF is responsible for any use that may be made of the Copernicus Information or the data it contains. DWD is acknowledged for providing the RADKLIM and REGNIE data. The WRF simulation was performed on the HPE Apollo Hawk national supercomputer at the High Performance Computing Center Stuttgart (HLRS) under the grant number ipm12835. The survey campaigns on extreme precipitation impacts were conducted and supported by the following projects/parties: in Lohmar and Hersbruck by the project "URBAS — Urban flash floods" (BMBF; 0330701C), in Osnabrueck by the University of Potsdam, the German Research Centre for Geosciences GFZ and the Deutsche Rueckversicherung AG, in Muenster and Greven by the project "EVUS — Real-time prediction of pluvial floods and induced water contamination in urban areas" (BMBF, 03G0846B), in Leegebruch 2017 by the project "ExTrass - Urban resilience against extreme weather events—typologies and transfer of adaptation strategies in small metropolises and medium-sized cities" (BMBF; 01LR1709A1) and in Berlin by the project "NatRiskChange - Natural hazards and risk in a changing world" (DFG; GRK 2043/2). MA and SM thank the Blitz-Informationsdienst von Siemens (BLIDS; namely Stephan Thern) for providing the lightning data. KB gratefully acknowledges the provision of computing time through the Center for Information Services and HPC (ZIH) at TU Dresden.

- Alfieri, L., Feyen, L., Dottori, F., and Bianchi, A.: Ensemble flood risk assessment in Europe under high end climate scenarios, *Global Environmental Change*, 35, 199–212, <https://doi.org/10.1016/j.gloenvcha.2015.09.004>, 2015.
- Allen, M.: Liability for climate change, *Nature*, 421, 891 – 892, <https://doi.org/10.1038/421891a>, 2003.
- Armon, M., Marra, F., Enzel, Y., Rostkier-Edelstein, D., Garfinkel, C. I., Adam, O., Dayan, U., and Morin, E.: Reduced Rainfall in Future Heavy Precipitation Events Related to Contracted Rain Area Despite Increased Rain Rate, *Earth’s Future*, 10, e2021EF002397, 2022.
- Baldauf, M., Seifert, A., Förstner, J., Majewski, D., Raschendorfer, M., and Reinhardt, T.: Operational Convective-Scale Numerical Weather Prediction with the COSMO Model: Description and Sensitivities, *Monthly Weather Review*, 139, 3887 – 3905, <https://doi.org/10.1175/MWR-D-10-05013.1>, 2011.
- Ban, N., Caillaud, C., Coppola, E., Pichelli, E., Sobolowski, S., Adinolfi, M., Ahrens, B., Alias, A., Anders, I., Bastin, S., Belušić, D., Berthou, S., Brisson, E., Cardoso, R., Chan, S., Christensen, O., Fernández, J., Fita, L., Frisius, T., Gašparac, G., Giorgi, F., Goergen, K., Haugen, J., Hodnebrog, Ø., Kartsios, S., Katragkou, E., Kendon, E., Keuler, K., Lavin-Gullon, A., Lenderink, G., Leutwyler, D., Lorenz, T., Maraun, D., Mercogliano, P., Milovac, J., Panitz, H.-J., Raffa, M., Remedio, A., Schär, C., Soares, P., Srncic, L., Steensen, B., Stocchi, P., Tölle, M., Truhetz, H., Vergara-Temprado, J., de Vries, H., Warrach-Sagi, K., Wulfmeyer, V., and Zander, M.: The first multi-model ensemble of regional climate simulations at kilometer-scale resolution, part I: evaluation of precipitation, *Clim Dyn*, 57, 275–302, <https://doi.org/10.1007/s00382-021-05708-w>, 2021.
- Bartels, H., Weigl, E., Reich, T., Lang, P., Wagner, A., Kohler, O., and Gerlach, N.: Projekt RADOLAN: Routineverfahren zur Online-Aneicherung der Radarniederschlagsdaten mit Hilfe von automatischen Bodenniederschlagsstationen (Ombrometer), Tech. rep., Deutscher Wetterdienst (DWD), <http://www.dwd.de/RADOLAN>, (in German), 2004.
- Barthlott, C. and Hoose, C.: Spatial and temporal variability of clouds and precipitation over Germany: multiscale simulations across the gray zone, *Atmospheric Chemistry and Physics*, 15, 12361–12384, <https://doi.org/10.5194/acp-15-12361-2015>, 2015.
- Berg, P., Wagner, S., Kunstmann, H., and Schädler, G.: High resolution regional climate model simulations for Germany: part I—validation, *Climate Dynamics*, 40, 401–414, <https://doi.org/10.1007/s00382-012-1508-8>, 2012.
- Berghäuser, L., Schoppa, L., Ulrich, J., Dillenardt, L., Jurado, O. E., Passow, C., Mohor, G. S., and Seleem, O.: Starkregen in Berlin - Meteorologische Ereignisrekonstruktion und Betroffenenbefragung, Tech. rep., University of Potsdam, Potsdam, <https://doi.org/10.25932/publishup-50056>, (in German), 2021.
- Bissolli, P. and Dittmann, E.: The objective weather type classification of the German Weather Service and its possibilities of application to environmental and meteorological investigations, *Meteorol. Z.*, pp. 253–260, <https://doi.org/10.1127/0941-2948/2001/0010-0253>, 2001.
- Bollmeyer, C., Keller, J. D., Ohlwein, C., Wahl, S., Crewell, S., Friederichs, P., Hense, A., Keune, J., Kneifel, S., Pscheidt, I., Redl, S., and Steinke, S.: Towards a high-resolution regional reanalysis for the European CORDEX domain, *Q. J. R. Meteorol. Soc.*, 141, 1–15, <https://doi.org/10.1002/qj.2486>, 2015.
- Bolton, D.: The computation of equivalent potential temperature, *Mon. Weather Rev.*, 108, 1046–1053, [https://doi.org/10.1175/1520-0493\(1980\)108<1046:TCOEPT>2.0.CO;2](https://doi.org/10.1175/1520-0493(1980)108<1046:TCOEPT>2.0.CO;2), 1980.
- Brieber, A. and Hoy, A.: Statistical analysis of very high-resolution precipitation data and relation to atmospheric circulation in Central Germany, *Adv. Sci. Res.*, <https://doi.org/10.24381/cds.adbb2d47>, 2018.

- 965 Bronstert, A., Agarwal, A., Boessenkool, B., Crisologo, I., Fischer, M., Heistermann, M., Köhn-Reich, L., López-Tarazón, J. A., Moran, T., Ozturk, U., Reinhardt-Imjela, C., and Wendi, D.: Forensic hydro-meteorological analysis of an extreme flash flood: The 2016-05-29 event in Braunsbach, SW Germany, *Sci. Total Environ.*, 630, 977–991, <https://doi.org/10.1016/j.scitotenv.2018.02.241>, 2018.
- Caldas-Alvarez, A., Khodayar, S., and Knippertz, P.: The impact of GPS and high-resolution radiosonde nudging on the simulation of heavy precipitation during HyMeX IOP6, *Weather and Climate Dynamics*, 2, 561–580, <https://doi.org/10.5194/wcd-2-561-2021>, 2021.
- 970 Caldas-Alvarez, A., Feldmann, H., Lucio-Eceiza, E., and Pinto, J. G.: Scale-dependency of extreme precipitation processes in regional climate simulations of the greater Alpine region, <https://doi.org/10.5194/wcd-2022-11>, 2022.
- Coles, S.: *An introduction to statistical modeling of extreme values*, Springer, London, UK, London [u.a.], 2001.
- Costa-Surós, M., Sourdeval, O., Acquistapace, C., Baars, H., Carbajal Henken, C., Genz, C., Hesemann, J., Jimenez, C., König, M., Kretzschmar, J., Madenach, N., Meyer, C. I., Schrödner, R., Seifert, P., Senf, F., Brueck, M., Cioni, G., Engels, J. F., Fieg, K., Gorges, K., Heinze, R., Siligam, P. K., Burkhardt, U., Crewell, S., Hoose, C., Seifert, A., Tegen, I., and Quaas, J.: Detection and attribution of aerosol-cloud interactions in large-domain large-eddy simulations with the ICOSahedral Non-hydrostatic model, *Atmos. Chem. Phys.*, 20, 5657–5678, <https://doi.org/10.5194/acp-20-5657-2020>, 2020.
- 975 Davison, A. and Huser, R.: Statistics of Extremes, *Annu. Rev. Stat. Appl.*, 2, 203–235, <https://doi.org/10.1146/annurev-statistics-010814-020133>, 2015.
- 980 Davolio, S., Fera, S. D., Laviola, S., Miglietta, M. M., and Levizzani, V.: Heavy Precipitation over Italy from the Mediterranean Storm “Vaia” in October 2018: Assessing the Role of an Atmospheric River, *Monthly Weather Review*, 148, 3571–3588, <https://doi.org/10.1175/mwr-d-20-0021.1>, 2020.
- Dillenaar, L., Hudson, P., and Thielen, A. H.: Urban pluvial flood adaptation: Results of a household survey across four German municipalities, *J. Flood Risk Manag.*, pp. 1–15, <https://doi.org/10.1111/jfr3.12748>, 2021.
- 985 Douville, H., Raghavan, K., Renwick, J., Allan, R., Arias, P., Barlow, M., Cerezo-Mota, R., Cherchi, A., Gan, T., Gergis, J., Jiang, D., Khan, A., Mba, W. P., Rosenfeld, D., Tierney, J., and Zolina, O.: Water Cycle Changes, in: *Climate Change 2021: The Physical Science Basis. Contribution of Working Group I to the Sixth Assessment Report of the Intergovernmental Panel on Climate Change*, edited by Masson-Delmotte, V., Zhai, P., Pirani, A., Connors, S., Péan, C., Berger, S., Caud, N., Chen, Y., Goldfarb, L., Gomis, M., Huang, M., Leitzell, K., Lonnoy, E., Matthews, J., Maycock, T., Waterfield, T., Yelekçi, O., Yu, R., and Zhou, B., chap. 8, Cambridge University Press, Cambridge, United Kingdom and New York, NY, USA, 2021.
- 990 Drobinski, P., Alonzo, B., Bastin, S., Silva, N. D., and Muller, C.: Scaling of precipitation extremes with temperature in the French Mediterranean region: What explains the hook shape?, *J. Geophys. Res. Atmos.*, 121, 3100–3119, <https://doi.org/10.1002/2015JD023497>, 2016.
- Drüe, C., Hauf, T., Finke, U., Keyn, S., and Kreyer, O.: Comparison of a SAFIR lightning detection network in northern Germany to the operational BLIDS network, *J. Geophys. Res. Atmos.*, 112, D18 114, <https://doi.org/10.1029/2006JD007680>, 2007.
- 995 DWA: DWA-Regelwerk: Merkblatt DWA-M 552 – Ermittlung von Hochwasserwahrscheinlichkeiten, Deutschen Vereinigung für Wasserwirtschaft, Abwasser und Abfall e.V. (DWA), Hennef, Germany., 2012.
- DWD: OpenData, Deutscher Wetterdienst (DWD), Available online: <https://opendata.dwd.de>, (accessed on 01 Nov 2021), n.d.
- Eden, J. M., Wolter, K., Otto, F. E., and Van Oldenborgh, G. J.: Multi-method attribution analysis of extreme precipitation in Boulder, Colorado, *Environmental Research Letters*, 11, 124 009, 2016.
- 1000 Efron, B. and Tibshirani, R. J.: *An introduction to the bootstrap*. Monographs on Statistics and Applied Probability 57, Chapman and Hall, New York, USA, 1993.

- Ehmele, F., Kautz, L.-A., Feldmann, H., and Pinto, J. G.: Long-term variance of heavy precipitation across central Europe using a large ensemble of regional climate model simulations, *Earth System Dynamics*, 11, 469–490, <https://doi.org/10.5194/esd-11-469-2020>, 2020.
- 1005 ESA: Land Cover CCI Product User Guide Version 2. Tech. Rep., Tech. rep., European Space Agency, http://maps.elie.ucl.ac.be/CCI/viewer/download/ESACCI-LC-Ph2-PUGv2_2.0.pdf, 2017.
- Fan, J., Rosenfeld, D., Yang, Y., Zhao, C., Leung, L. R., and Li, Z.: Substantial contribution of anthropogenic air pollution to catastrophic floods in Southwest China, *Geophys. Res. Lett.*, 42, 6066–6075, <https://doi.org/10.1002/2015GL064479>, 2015.
- Fauer, F. S., Ulrich, J., Jurado, O. E., and Rust, H. W.: Flexible and Consistent Quantile Estimation for Intensity-Duration-Frequency Curves, *Hydrol. Earth Syst. Sci. Discuss.*, 2021, 1–23, <https://doi.org/10.5194/hess-2021-334>, 2021.
- 1010 Ferro, C. A. T. and Stephenson, D. B.: Extremal Dependence Indices: Improved Verification Measures for Deterministic Forecasts of Rare Binary Events, *Weather Forecast.*, 26, 699 – 713, <https://doi.org/10.1175/WAF-D-10-05030.1>, 2011.
- Formayer, H. and Fritz, A.: Temperature dependency of hourly precipitation intensities–surface versus cloud layer temperature, *Int. J. Climatol.*, 37, 1–10, <https://doi.org/10.1002/joc.4678>, 2017.
- Forum, W. E.: The Global Risks Report 2020, http://www3.wefo-rum.org/docs/WEF_Global_Risk_Report_2020.pdf, 2020.
- 1015 Fossier, G., Khodayar, S., and Berg, P.: Benefit of convection permitting climate model simulations in the representation of convective precipitation, *Climate Dynamics*, 44, 45–60, <https://doi.org/10.1007/s00382-014-2242-1>, 2014.
- Ganguli, P. and Coulibaly, P.: Does nonstationarity in rainfall require nonstationary intensity–duration–frequency curves?, *Hydrol. Earth Syst. Sci.*, 21, 6461–6483, <https://doi.org/10.5194/hess-21-6461-2017>, 2017.
- GDV: Naturgefahrenreport 2018. Die Schaden-Chronik der deutschen Versicherer, Tech. rep., German Insurance Association, Berlin., uRL: <https://www.gdv.de/resource/blob/36254/23ad47bd6746bc456849b5cd41f61516/naturgefahrenreport-2018---schaden-chronik-data.pdf>, 2018.
- 1020 GDV: Serviceteil zum Naturgefahrenreport 2020, Tech. rep., German Insurance Association, Berlin., uRL: <https://www.gdv.de/resource/blob/63612/9bf0708f9a0017e98b878078894c7e52/naturgefahrenreport-2020---serviceteil-data.pdf>, 2020.
- GDV: Von 2002 bis 2017: Deutschlandweit 6,7 Milliarden Euro Starkregen-Schäden, uRL: <https://www.gdv.de/de/themen/news/von-2002-bis-2017--deutschlandweit-6-7-milliarden-euro-starkregen-schaeden--52762>, 2021.
- 1025 Gebauer, P., Myrcik, G., and Schenk, F.: Beiträge zur Berliner Wetterkarte. Herausgegeben vom Verein BERLINER WETTERKARTE e.V., Tech. rep., Institut für Meteorologie der Freien Universität Berlin, 2017.
- German Research Centre for Geosciences GFZ: HOWAS 21 - Flood Damage Database, <https://doi.org/10.1594/GFZ.SDDB.HOWAS21>, 2022.
- 1030 Gochis, D., Schumacher, R., Friedrich, K., Doesken, N., Kelsch, M., Sun, J., Ikeda, K., Lindsey, D., Wood, A., Dolan, B., et al.: The great Colorado flood of September 2013, *Bulletin of the American Meteorological Society*, 96, 1461–1487, 2015.
- Grams, C. M., Binder, H., Pfahl, S., Piaget, N., and Wernli, H.: Atmospheric processes triggering the central European floods in June 2013, *Nat. Hazards Earth Syst. Sci.*, 14, 1691–1702, <https://doi.org/10.5194/nhess-14-1691-2014>, 2014.
- Grieser, J., Staeger, T., and Schonwiese, C.-D.: Estimates and uncertainties of return periods of extreme daily precipitation in Germany, *Meteorol. Z.*, 16, 553–564, <https://doi.org/10.1127/0941-2948/2007/0235>, 2007.
- 1035 Gumbel, E. J.: *Statistics of Extremes*, Columbia University Press, New York, USA, 1958.
- Guo, J., Luo, Y., Yang, J., Furtado, K., and Lei, H.: Effects of anthropogenic and sea salt aerosols on a heavy rainfall event during the early-summer rainy season over coastal Southern China, *Atmospheric Research*, 265, 105 923, <https://doi.org/https://doi.org/10.1016/j.atmosres.2021.105923>, 2022.

- 1040 Hastings, D. A., Dunbar, P. K., Elphinstone, G. M., Bootz, M., Murakami, H., Maruyama, H., Masaharu, H., Holland, P., Payne, J., Bryant, N. A., Logan, T. L., Muller, J.-P., Schreier, G., and MacDonald, J. S.: The Global Land One-kilometer Base Elevation (GLOBE) Digital Elevation Model, Version 1.0., <http://www.ngdc.noaa.gov/mgg/topo/globe.html>, 1999.
- Hersbach, H., Bell, B., Berrisford, P., Biavati, G., Horányi, A., Muñoz Sabater, J., Nicolas, J., Peubey, C., Radu, R., Rozum, I., Schepers, D., Simmons, A., Soci, C., Dee, D., and Thépaut, J.-N.: ERA5 hourly data on single levels from 1979 to present, <https://doi.org/10.24381/cds.adbb2d47>, accessed on 11 Nov. 2021, 2018.
- 1045 Hersbach, H., Bell, B., Berrisford, P., Hirahara, S., Horányi, A., Muñoz-Sabater, J., Nicolas, J., Peubey, C., Radu, R., Schepers, D., Simmons, A., Soci, C., Abdalla, S., Abellan, X., Balsamo, G., Bechtold, P., Biavati, G., Bidlot, J., Bonavita, M., De Chiara, G., Dahlgren, P., Dee, D., Diamantakis, M., Dragani, R., Flemming, J., Forbes, R., Fuentes, M., Geer, A., Haimberger, L., Healy, S., Hogan, R. J., Hólm, E., Janisková, M., Keeley, S., Laloyaux, P., Lopez, P., Lupu, C., Radnoti, G., de Rosnay, P., Rozum, I., Vamborg, F., Villaume, S., and Thépaut, J.-N.: The ERA5 global reanalysis, *Q. J. R. Meteorol. Soc.*, 146, 1999–2049, <https://doi.org/10.1002/qj.3803>, 2020.
- 1050 Hibino, K., Takayabu, I., Wakazuki, Y., and Ogata, T.: Physical responses of convective heavy rainfall to future warming condition: Case study of the Hiroshima event, *Front. Environ. Sci.*, 6, 35, <https://doi.org/10.3389/feart.2018.00035>, 2018.
- Hogan, R. J., O'Connor, E. J., and Illingworth, A. J.: Verification of cloud-fraction forecasts, *Q. J. R. Meteorol. Soc.*, 135, 1494–1511, <https://doi.org/https://doi.org/10.1002/qj.481>, 2009.
- 1055 Hu, G. and Franzke, C. L. E.: Evaluation of Daily Precipitation Extremes in Reanalysis and Gridded Observation-Based Data Sets Over Germany, *Geophys. Res. Lett.*, 47, e2020GL089624, <https://doi.org/https://doi.org/10.1029/2020GL089624>, 2020.
- Hydrotec, University of Applied Sciences Aachen, and DWD: Vorhersage und Management von Sturzfluten in urbanen Gebieten (URBAS), Tech. rep., Aachen, uRL: http://www.urbanesturzfluten.de/schlussbericht/fallstudienHamburgbisLohmar/view?set_language=en, 2008.
- Jurado, O. E., Ulrich, J., Scheibel, M., and Rust, H. W.: Evaluating the performance of a max-stable process for estimating intensity-duration-frequency curves, *Water*, 12, 3314, <https://doi.org/10.3390/w12123314>, 2020.
- 1060 Kadow, C., Illing, S., Lucio-Eceiza, E. E., Bergemann, M., Ramadoss, M., Sommer, P. S., Kunst, O., Schartner, T., Pankatz, K., Grieger, J., et al.: Introduction to Freva – A Free Evaluation System Framework for Earth System Modeling, *J. Open Res. Softw.*, 9, 1–13, <https://doi.org/10.5334/jors.253>, 2021.
- Kaiser, M., Günemann, S., and Disse, M.: Spatiotemporal analysis of heavy rain-induced flood occurrences in Germany using a novel event database approach, *J. Hydrol.*, 595, 125985, <https://doi.org/10.1016/j.jhydrol.2021.125985>, 2021.
- 1065 Kaspar, F., Müller-Westermeier, G., Penda, E., Mächel, H., Zimmermann, K., Kaiser-Weiss, A., and Deutschländer, T.: Monitoring of climate change in Germany – data, products and services of Germany's National Climate Data Centre, *Adv. Sci. Res.*, 10, 99–106, <https://doi.org/10.5194/asr-10-99-2013>, 2013.
- Kelemen, F. D., Ludwig, P., Reyers, M., Ulbrich, S., and Pinto, J. G.: Evaluation of moisture sources for the Central European summer flood of May/June 2013 based on regional climate model simulations, *Tellus A: Dyn. Meteorol. Oceanogr.*, 68, 29288, <https://doi.org/10.3402/tellusa.v68.29288>, 2016.
- 1070 Keller, J. D. and Wahl, S.: Representation of climate in reanalyses: An intercomparison for Europe and North America, *J. Climate*, 34, 1667–1684, <https://doi.org/10.1175/JCLI-D-20-0609.1>, 2021.
- Kendon, E. J., Roberts, N. M., Senior, C. A., and Roberts, M. J.: Realism of rainfall in a very high-resolution regional climate model, *J. Climate*, 25, 5791–5806, <https://doi.org/10.1175/JCLI-D-11-00562.1>, 2012.
- 1075 Kharin, V. V. and Zwiers, F. W.: Changes in the extremes in an ensemble of transient climate simulations with a coupled atmosphere-ocean GCM, *J. Climate*, 13, 3760–3788, [https://doi.org/10.1175/1520-0442\(2000\)013<3760:CITEIA>2.0.CO;2](https://doi.org/10.1175/1520-0442(2000)013<3760:CITEIA>2.0.CO;2), 2000.

- 1080 Khodayar, S., Davolio, S., Girolamo, P. D., Brossier, C. L., Flaounas, E., Fourrie, N., Lee, K.-O., Ricard, D., Vie, B., Bouttier, F., Caldas-Alvarez, A., and Ducrocq, V.: Overview towards improved understanding of the mechanisms leading to heavy precipitation in the western Mediterranean: lessons learned from HyMeX, *Atmospheric Chemistry and Physics*, 21, 17 051–17 078, <https://doi.org/10.5194/acp-21-17051-2021>, 2021.
- Koutsoyiannis, D., Kozonis, D., and Manetas, A.: A mathematical framework for studying rainfall intensity-duration-frequency relationships, *J. Hydrol.*, 206, 118–135, [https://doi.org/10.1016/S0022-1694\(98\)00097-3](https://doi.org/10.1016/S0022-1694(98)00097-3), 1998.
- 1085 Kox, T. and Lüder, C.: Impacts as triggers for weather-related decision making: Observations at the Berlin Fire Brigade Control and Dispatch Center, *Int. J. Disaster Risk Sci.*, <https://doi.org/10.1007/s13753-021-00356-4>, 2021.
- Kreibich, H., Müller, M., Thielen, A. H., and Merz, B.: Flood precaution of companies and their ability to cope with the flood in August 2002 in Saxony, Germany, *Water Resour. Res.*, 43, <https://doi.org/10.1029/2005WR004691>, 2007.
- 1090 Kreienkamp, F., Philip, S. Y., Tradowsky, J. S., Kew, S. F., Lorenz, P., Arrighi, J., Belleflamme, A., Bettmann, T., Caluwaerts, S., Chan, S. C., Ciavarella, A., De Cruz, L., de Vries, H., Demuth, N., Ferrone, A., Fischer, E. M., Fowler, H. J., Goergen, K., Heinrich, D., Henrichs, Y., Lenderink, G., Kaspar, F., Nilson, E., Otto, F. E. L., Ragone, F., Seneviratne, S. I., Singh, R. K., Skålevåg, A., Termonia, P., Thalheimer, L., van Aalst, M., Van den Bergh, J., Van de Vyver, H., Vannitsem, S., van Oldenborgh, G. J., Van Schaeybroeck, B., Vautard, R., Vonk, D., and Wanders, N.: Rapid attribution of heavy rainfall events leading to the severe flooding in Western Europe during July 2021, Tech. rep., World Weather Attribution, <https://www.worldweatherattribution.org/wp-content/uploads/Scientific-report-Western-Europe-floods-2021-attribution.pdf>, 2021.
- 1095 Kron, W.: Flood Risk = Hazard • Values • Vulnerability, *Water International*, 30, 58–68, <https://doi.org/10.1080/02508060508691837>, 2005.
- Kröner, N.: Identifying and quantifying large-scale drivers of European climate change, Ph.D. thesis, ETH Zurich, 2016.
- Kröner, N., Kotlarski, S., Fischer, E., Lüthi, D., Zubler, E., and Schär, C.: Separating climate change signals into thermodynamic, lapse-rate and circulation effects: theory and application to the European summer climate, *Clim. Dynam.*, 48, 3425–3440, <https://doi.org/10.1007/s00382-016-3276-3>, 2017.
- 1100 Kuhlicke, C., Seebauer, S., Hudson, P., Begg, C., Bubeck, P., Dittmer, C., Grothmann, T., Heidenreich, A., Kreibich, H., Lorenz, D. F., Masson, T., Reiter, J., Thaler, T., Thielen, A. H., and Bamberg, S.: The behavioral turn in flood risk management, its assumptions and potential implications, *WIREs Water*, 7, 1–22, <https://doi.org/10.1002/wat2.1418>, 2020.
- Kunz, M., Mühr, B., Kunz-Plapp, T., Daniell, J., Khazai, B., Wenzel, F., Vannieuwenhuysse, M., Comes, T., Elmer, F., Schröter, K., et al.: Investigation of superstorm Sandy 2012 in a multi-disciplinary approach, *Natural Hazards and Earth System Sciences*, 13, 2579–2598, 2013.
- 1105 Lackmann, G. M.: Hurricane Sandy before 1900 and after 2100, *Bull. Am. Meteorol. Soc.*, 96, 547–560, <https://doi.org/10.1175/BAMS-D-14-00123.1>, 2015.
- Leckebusch, G. C., Renggli, D., and Ulbrich, U.: Development and application of an objective storm severity measure for the Northeast Atlantic region, *Meteorol. Z.*, 17, 575–587, <https://doi.org/10.1127/0941-2948/2008/0323>, 2008.
- 1110 Lengfeld, K., Kirstetter, P.-E., Fowler, H. J., Yu, J., Becker, A., Flamig, Z., and Gourley, J.: Use of radar data for characterizing extreme precipitation at fine scales and short durations, *Environ. Res. Lett.*, 15, 085 003, <https://doi.org/10.1088/1748-9326/ab98b4>, 2020.
- Lengfeld, K., Walawender, E., Winterrath, T., and Becker, A.: CatRaRE: A Catalogue of radar-based heavy rainfall events in Germany derived from 20 years of data, *Meteorol. Z.*, <https://doi.org/10.1127/metz/2021/1088>, 2021a.

- Lengfeld, K., Walawender, E., Winterrath, T., Weigl, E., and Becker, A.: Heavy precipitation events Version 2021.01 exceeding DWD warning level 3 for severe weather based on RADKLIM-RW Version 2017.002, https://doi.org/10.5676/DWD/CatRaRE_W3_Eta_v2021.01, 2021b.
- 1115 Liu, Z., Ming, Y., Zhao, C., Lau, N. C., Guo, J., Bollasina, M., and Yim, S. H. L.: Contribution of local and remote anthropogenic aerosols to a record-breaking torrential rainfall event in Guangdong Province, China, *Atmos. Chem. Phys.*, 20, 223–241, <https://doi.org/10.5194/acp-20-223-2020>, 2020.
- 1120 Lucas-Picher, P., Argüeso, D., Brisson, E., Trambly, Y., Berg, P., Lemonsu, A., Kotlarski, S., and Caillaud, C.: Convection-permitting modeling with regional climate models: Latest developments and next steps, *WIREs Climate Change*, 12, e731, <https://doi.org/10.1002/wcc.731>, 2021.
- Maity, R.: *Statistical methods in hydrology and hydroclimatology*, Springer Nature Singapore Pte Ltd., Singapore, <https://doi.org/10.1007/978-981-10-8779-0>, 2018.
- 1125 Makkonen, L.: Plotting positions in extreme value analysis, *J. Appl. Meteorol. Climatol.*, 45, 334–340, <https://doi.org/10.1175/JAM2349.1>, 2006.
- Markowski, P. and Richardson, Y.: *Mesoscale Convective Systems*, chap. 9, pp. 245–272, John Wiley & Sons, Ltd, <https://doi.org/https://doi.org/10.1002/9780470682104.ch9>, 2010.
- Martens, B., Schumacher, D. L., Wouters, H., Muñoz-Sabater, J., Verhoest, N. E. C., and Miralles, D. G.: Evaluating the land-surface energy partitioning in ERA5, *Geoscientific Model Development*, 13, 4159–4181, <https://doi.org/10.5194/gmd-13-4159-2020>, 2020.
- 1130 Meredith, E. P., Ulbrich, U., and Rust, H. W.: Subhourly rainfall in a convection-permitting model, *Environ. Res. Lett.*, 15, 034031, <https://doi.org/10.1088/1748-9326/ab6787>, 2020.
- Meredith, E. P., Ulbrich, U., Rust, H. W., and Truhetz, H.: Present and future diurnal hourly precipitation in 0.11° EURO-CORDEX models and at convection-permitting resolution, *Environ. Res. Commun.*, 3, 055002, <https://doi.org/10.1088/2515-7620/abf15e>, 2021.
- 1135 Merz, B., Kreibich, H., Schwarze, R., and Thielen, A. H.: Review article "Assessment of economic flood damage", *Natural Hazards and Earth System Science*, 10, 1697–1724, <https://doi.org/10.5194/nhess-10-1697-2010>, 2010.
- Milrad, S. M., Gyakum, J. R., and Atallah, E. H.: A meteorological analysis of the 2013 Alberta flood: Antecedent large-scale flow pattern and synoptic–dynamic characteristics, *Monthly Weather Review*, 143, 2817–2841, 2015.
- Mohr, S., Wilhelm, J., Wandel, J., Kunz, M., Portmann, R., Punge, H. J., Schmidberger, M., Quinting, J. F., and Grams, C. M.: The role of large-scale dynamics in an exceptional sequence of severe thunderstorms in Europe May–June 2018, *Wea. Clim. Dyn.*, 1, 325–348, <https://doi.org/10.5194/wcd-1-325-2020>, 2020.
- 1140 Mohr, S., Ehret, U., Kunz, M., Ludwig, P., Caldas-Alvarez, A., Daniell, J. E., Ehmele, F., Feldmann, H., Franca, M. J., Gattke, C., Hundhausen, M., Knippertz, P., Küpfer, K., Mühr, B., Pinto, J. G., Quinting, J., Schäfer, A. M., Scheibel, M., Seidel, F., and Wisotzky, C.: A multi-disciplinary analysis of the exceptional flood event of July 2021 in central Europe. Part 1: Event description and analysis, *Natural Hazards and Earth System Sciences Discussions*, 2022, 1–44, <https://doi.org/10.5194/nhess-2022-137>, 2022.
- 1145 Mélése, V., Blanchet, J., and Molinié, G.: Uncertainty estimation of Intensity–Duration–Frequency relationships: A regional analysis, *J. Hydrol.*, 558, 579–591, <https://doi.org/https://doi.org/10.1016/j.jhydrol.2017.07.054>, 2018.
- Nakanishi, M. and Niino, H.: An Improved Mellor Yamada Level-3 Model: Its Numerical Stability and Application to a Regional Prediction of Advection Fog, *Boundary Layer Meteorol.*, 119, 397–407, <https://doi.org/10.1007/s10546-005-9030-8>, 2006.
- 1150 Nakanishi, M. and Niino, H.: Development of an Improved Turbulence Closure Model for the Atmospheric Boundary Layer, *Japan J. Meteorol. Soc.*, 87, 895–912, <https://doi.org/10.2151/jmsj.87.895>, 2009.

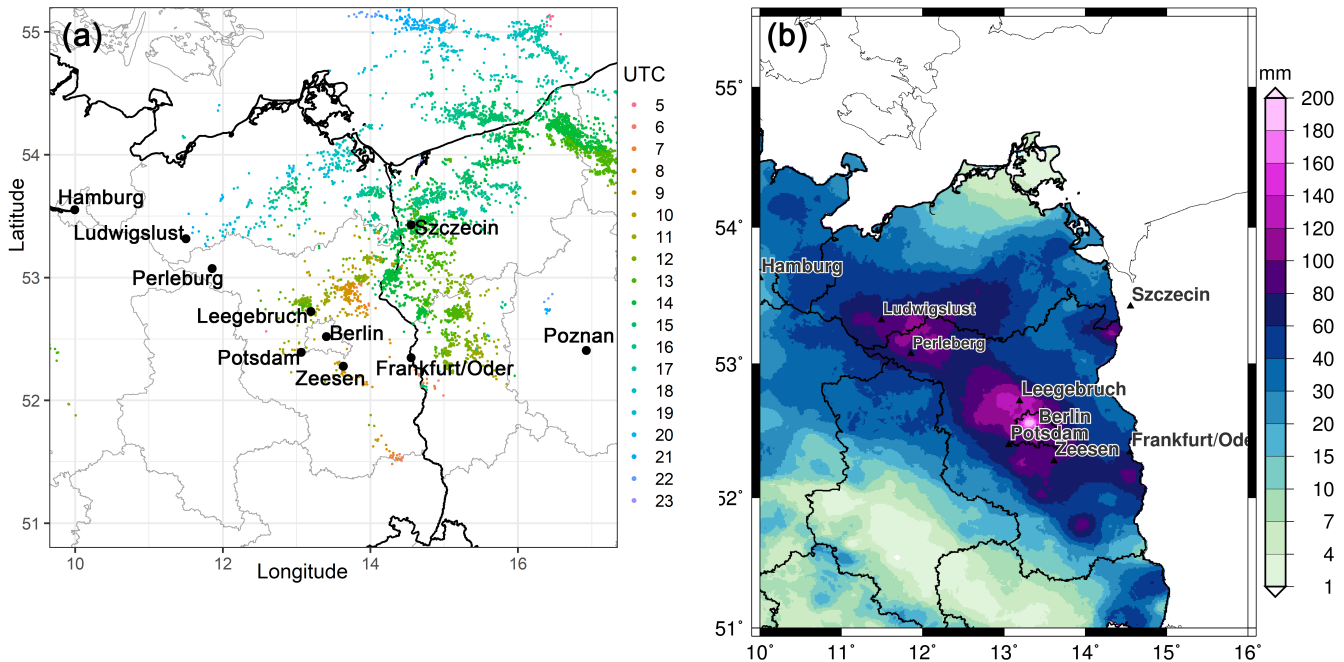
- Noyelle, R., Ulbrich, U., Becker, N., and Meredith, E. P.: Assessing the impact of sea surface temperatures on a simulated medicane using ensemble simulations, *Nat. Hazards Earth Syst. Sci.*, 19, 941–955, <https://doi.org/10.5194/nhess-19-941-2019>, 2019.
- 1155 Olson, J. B., Kenyon, J., Angevine, W., Brown, J., Pagowski, M., and Suselj, K.: A Description of the MYNN-EDMF Scheme and the Coupling to Other Components in WRF–ARW, NOAA Technical Memorandum OAR GSD 61, NOAA, Boulder/CO., <https://repository.library.noaa.gov/view/noaa/19837>, 2019.
- O’Neill, B. C., Tebaldi, C., Vuuren, D. P. v., Eyring, V., Friedlingstein, P., Hurtt, G., Knutti, R., Kriegler, E., Lamarque, J.-F., Lowe, J., et al.: The scenario model intercomparison project (ScenarioMIP) for CMIP6, *Geosci. Model Dev.*, 9, 3461–3482, <https://doi.org/10.5194/gmd-9-3461-2016>, 2016.
- 1160 Otto, F. E. L.: Attribution of weather and climate events, *Annu. Rev. Environ. Res.*, 42, 627–646, <https://doi.org/10.1146/annurev-environ-102016-060847>, 2017.
- Pall, P., Patricola, C. M., Wehner, M. F., Stone, D. A., Paciorek, C. J., and Collins, W. D.: Diagnosing conditional anthropogenic contributions to heavy Colorado rainfall in September 2013, *Wea. Clim. Extrem.*, 17, 1–6, <https://doi.org/10.1016/j.wace.2017.03.004>, 2017.
- Papalexiou, S. M. and Koutsoyiannis, D.: Battle of extreme value distributions: A global survey on extreme daily rainfall, *Water Resour. Res.*, 49, 187–201, <https://doi.org/10.1029/2012WR012557>, 2013.
- 1165 Philip, S., Kew, S. F., Jan van Oldenborgh, G., Aalbers, E., Vautard, R., Otto, F., Haustein, K., Habets, F., and Singh, R.: Validation of a rapid attribution of the May/June 2016 flood-inducing precipitation in France to climate change, *J. Hydrol.*, 19, 1881–1898, <https://doi.org/10.1175/JHM-D-18-0074.1>, 2018.
- Philip, S., Kew, S., van Oldenborgh, G. J., Otto, F., Vautard, R., van der Wiel, K., King, A., Lott, F., Arrighi, J., Singh, R., and van Aalst, M.: A protocol for probabilistic extreme event attribution analyses, *Adv. Stat. Clim. Meteorol. Oceanogr.*, <https://doi.org/10.5194/ascmo-6-177-2020>, 2020.
- 1170 Pichelli, E., Coppola, E., Sobolowski, S., Ban, N., Giorgi, F., Stocchi, P., Alias, A., Belušić, D., Berthou, S., Caillaud, C., Cardoso, R. M., Chan, S., Christensen, O. B., Dobler, A., de Vries, H., Goergen, K., Kendon, E. J., Keuler, K., Lenderink, G., Lorenz, T., Mishra, A. N., Panitz, H.-J., Schär, C., Soares, P. M. M., Truhetz, H., and Vergara-Temprado, J.: The first multi-model ensemble of regional climate simulations at kilometer-scale resolution part 2: historical and future simulations of precipitation, *Climate Dynamics*, 56, 3581–3602, <https://doi.org/10.1007/s00382-021-05657-4>, 2021.
- Pinto, J. G., Karremann, M. K., Born, K., Della-Marta, P. M., and Klawa, M.: Loss potentials associated with European windstorms under future climate conditions, *Clim. Res.*, 54, 1–20, <https://doi.org/10.3354/cr01111>, 2012.
- Piper, D. and Kunz, M.: Spatiotemporal variability of lightning activity in Europe and the relation to the North Atlantic Oscillation teleconnection pattern, *Nat. Hazards Earth Syst. Sci.*, 17, 1319–1336, <https://doi.org/10.5194/nhess-17-1319-2017>, 2017.
- 1180 Piper, D., Kunz, M., Ehmele, F., Mohr, S., Mühr, B., Kron, A., and Daniell, J.: Exceptional sequence of severe thunderstorms and related flash floods in May and June 2016 in Germany. Part I: Meteorological background, *Nat. Hazards Earth Syst. Sci.*, 16, 2835–2850, <https://doi.org/10.5194/nhess-16-2835-2016>, 2016.
- Poelman, D. R., Schulz, W., Diendorfer, G., and Bernardi, M.: The European lightning location system EUCLID – Part 2: Observations, *Nat. Hazards Earth Syst. Sci.*, 16, 607–616, <https://doi.org/10.5194/nhess-16-607-2016>, 2016.
- 1185 Poggio, L., de Sousa, L. M., Batjes, N. H., Heuvelink, G. B. M., Kempen, B., Ribeiro, E., and Rossiter, D.: SoilGrids 2.0: producing soil information for the globe with quantified spatial uncertainty, *Soil*, 7, 217–240, <https://doi.org/10.5194/soil-7-217-2021>, 2021.
- Prein, A., Gobiet, A., Suklitsch, M., Truhetz, H., Awan, N., Keuler, K., and Georgievski, G.: Added value of convection permitting seasonal simulations, *Clim Dyn*, 41, 2655–2677, <https://doi.org/10.1007/s00382-013-1744-6>, 2013.

- 1190 Prein, A. F., Langhans, W., Fosser, G., Ferrone, A., Ban, N., Goergen, K., Keller, M., Tölle, M., Gutjahr, O., Feser, F., Brisson, E., Kollet, S., Schmidli, J., van Lipzig, N. P. M., and Leung, R.: A review on regional convection-permitting climate modeling: Demonstrations, prospects, and challenges, *Reviews of Geophysics*, 53, 323–361, <https://doi.org/10.1002/2014RG000475>, 2015.
- Purr, C., Brisson, E., and Ahrens, B.: Convective rain cell characteristics and scaling in climate projections for Germany, *Int. J. Climatol.*, 41, 3174–3185, <https://doi.org/10.1002/joc.7012>, 2021.
- 1195 Rauthe, M., Steiner, H., Riediger, U., A., M., and Gratzki, A.: A Central European precipitation climatology -- Part I: Generation and validation of a high-resolution gridded daily data set (HYRAS), *Meteorol. Z.*, 22, 235–256, <https://doi.org/10.1127/0941-2948/2013/0436>, 2013.
- Rezacova, D., Zacharov, P., and Sokol, Z.: Uncertainty in the area-related QPF for heavy convective precipitation, *Atmos. Res.*, 93, 238–246, <https://doi.org/10.1016/j.atmosres.2008.12.005>, 2009.
- 1200 Rockel, B., Will, A., and Hense, A.: The regional climate model COSMO-CLM (CCLM), *Meteorol. Z.*, 17, 347–348, <https://doi.org/10.1127/0941-2948/2008/0309>, 2008.
- Rosenfeld, D., Andreae, M. O., Asmi, A., Chin, M., de Leeuw, G., Donovan, D. P., Kahn, R., Kinne, S., Kivekäs, N., Kulmala, M., Lau, W., Schmidt, S., Suni, T., Wagner, T., Wild, M., and Quaas, J.: Global observations of aerosol-cloud-precipitation-climate interactions, *Reviews Geophys.*, 52, 750–808, <https://doi.org/10.1002/2013RG000441>, 2014.
- 1205 Rözer, V., Müller, M., Bubeck, P., Kienzler, S., Thieken, A., Pech, I., Schröter, K., Buchholz, O., and Kreibich, H.: Coping with pluvial floods by private households, *Water*, 8, 304, <https://doi.org/10.3390/W8070304>, 2016.
- Rözer, V., Kreibich, H., Schröter, K., Müller, M., Sairam, N., Doss-Gollin, J., Lall, U., and Merz, B.: Probabilistic Models Significantly Reduce Uncertainty in Hurricane Harvey Pluvial Flood Loss Estimates, *Earth's Future*, 7, 384–394, <https://doi.org/10.1029/2018EF001074>, 2019.
- 1210 Rust, H. W.: The effect of long-range dependence on modelling extremes with the generalised extreme value distribution, *Eur. Phys. J. Spec. Top.*, 174, 91–97, <https://doi.org/10.1140/epjst/e2009-01092-8>, 2009.
- Schär, C., Frei, C., Lüthi, D., and Davies, H. C.: Surrogate climate-change scenarios for regional climate models, *Geophys. Res. Lett.*, 23, 669–672, <https://doi.org/10.1029/96GL00265>, 1996.
- Schulz, W., Diendorfer, G., Pedebay, S., and Poelman, D. R.: The European lightning location system EUCLID – Part 1: Performance analysis and validation, *Nat. Hazards Earth Syst. Sci.*, 16, 595–605, <https://doi.org/10.5194/nhess-16-595-2016>, 2016.
- 1215 Schwitalla, T., Warrach-Sagi, K., Wulfmeyer, V., and Resch, M.: Near-global-scale high-resolution seasonal simulations with WRF-Noah-MP v.3.8.1, *Geosci. Model Dev.*, 13, 1959–1974, <https://doi.org/10.5194/gmd-13-1959-2020>, 2020.
- Schwitalla, T., Bauer, H.-S., Warrach-Sagi, K., Bönisch, T., and Wulfmeyer, V.: Turbulence-permitting air pollution simulation for the Stuttgart metropolitan area, *Atmos. Chem. Phys.*, 21, 4575–4597, <https://doi.org/10.5194/acp-21-4575-2021>, 2021.
- 1220 Sebastian, A., Gori, A., Blessing, R. B., van der Wiel, K., and Bass, B.: Disentangling the impacts of human and environmental change on catchment response during Hurricane Harvey, *Environ. Res. Lett.*, 14, 124 023, <https://doi.org/10.1088/1748-9326/ab5234>, 2019.
- Simmer, C., Adrian, G., Jones, S., Wirth, V., Göber, M., Hohenegger, C., Janjic ´, T., Keller, J., Ohlwein, C., Seifert, A., Trömel, S., Ulbrich, T., Wapler, K., Weissmann, M., Keller, J., Masbou, M., Meilinger, S., Riß, N., Schomburg, A., Vormann, A., and Weingärtner, C.: HErZ: The German Hans-Ertel Centre for Weather Research, *Bulletin of the American Meteorological Society*, 97, 1057–1068, <https://doi.org/10.1175/bams-d-13-00227.1>, 2016.
- 1225

- Skamarock, W. C., Klemp, J. B., Dudhia, J., Gill, D., Liu, Z., Berner, J., Wang, W., Duda, M. G., Powers, J. G., Barker, D., and Huang, X.-Y.: A Description of the Advanced Research WRF Version 4, NCAR Technical Note TN-556+STR, NCAR, Boulder/CO., <https://doi.org/10.5065/1dfh-6p97>, <https://opensky.ucar.edu/islandora/object/opensky:2898>, 2021.
- 1230 Smith, B. K., Smith, J. A., Baeck, M. L., and Miller, A. J.: Exploring storage and runoff generation processes for urban flooding through a physically based watershed model, *Water Resources Research*, 51, 1552–1569, <https://doi.org/10.1002/2014WR016085>, 2015.
- Sodemann, H., Schwierz, C., and Wernli, H.: Interannual variability of Greenland winter precipitation sources: Lagrangian moisture diagnostic and North Atlantic Oscillation influence, *J. Geophys. Res. Atmos.*, 113, <https://doi.org/10.1029/2007JD008503>, 2008.
- Song, H. and Sohn, B.: An Evaluation of WRF Microphysics Schemes for Simulating the Warm-Type Heavy Rain over the Korean Peninsula, *Asia-Pacific J. Atmos. Sci.*, 54, 225–236, <https://doi.org/10.1007/s13143-018-0006-2>, 2018.
- 1235 Spekkers, M., Rözer, V., Thielen, A., Ten Veldhuis, M. C., and Kreibich, H.: A comparative survey of the impacts of extreme rainfall in two international case studies, *Nat. Hazards Earth Syst. Sci.*, 17, 1337–1355, <https://doi.org/10.5194/nhess-17-1337-2017>, 2017.
- Spekkers, M. H., Kok, M., Clemens, F. H., and Ten Veldhuis, J. A.: Decision-tree analysis of factors influencing rainfall-related building structure and content damage, *Natural Hazards and Earth System Sciences*, 14, 2531–2547, <https://doi.org/10.5194/nhess-14-2531-2014>, 2014.
- 1240 Steinacker, R., Dorninger, M., Wölfelmaier, F., and Krennert, T.: Automatic tracking of convective cells and cell complexes from lightning and radar data, *Meteorol. Atmos. Phys.*, 72, 101–110, <https://doi.org/10.1007/s007030050009>, 2000.
- Stevens, B., Acquistapace, C., Hansen, A., Heinze, R., Klinger, C., Klocke, D., Schubotz, W., Windmiller, J., Adamidis, P., Arka, I., Barlakas, V., Biercamp, J., Brueck, M., Brune, S., Buehler, S., Burkhardt, U., Cioni, G., Costa-Surós, M., Crewell, S., Crueger, T., Deneke, H., Friederichs, P., Cintia Carbajal H., Hohenegger, C., Jacob, M., Jakub, F., Kalthoff, N., Köhler, M., Thirza W. van L., Li, P., Löhnert, U.,
- 1245 Macke, A., Madenach, N., Mayer, B., Nam, C., Naumann, A. K., Peters, K., Poll, S., Quaas, J., Röber, N., Rochetin, N., Rybka, H., Scheck, L., Schemann, V., Schnitt, S., Seifert, A., Senf, F., Shapkalijeviski, M., Simmer, C., Singh, S., Sourdeval, O., Spickermann, D., Strandgren, J., Tessiot, O., Vercauteren, N., Vial, J., Voigt, A., and Zängl, G.: Large-eddy and storm resolving models for climate prediction - the added value for clouds and precipitation, *J. Meteorol. Soc. Japan*, 98, <https://doi.org/10.2151/jmsj.2020-021>, 2020.
- Stott, P. A., Stone, D. A., and Allen, M. R.: Human contribution to the European heatwave of 2003, *Nature*, 432, 610–614, <https://doi.org/10.1038/nature03089>, 2004.
- 1250 Svensson, C. and Jones, D. A.: Review of rainfall frequency estimation methods, *J. Flood Risk Manag.*, 3, 296–313, <https://doi.org/10.1111/j.1753-318X.2010.01079.x>, 2010.
- Thompson, G. and Eidhammer, T.: A Study of Aerosol Impacts on Clouds and Precipitation Development in a Large Winter Cyclone, *Journal of the Atmospheric Sciences*, 71, 3636 – 3658, <https://doi.org/10.1175/JAS-D-13-0305.1>, 2014.
- 1255 Tiedtke, M.: A comprehensive mass flux scheme for cumulus parameterization in large-scale models, *Mon. Weather Rev.*, 117, 1779–1800, 1989.
- Trenberth, K. E., Fasullo, J. T., and Shepherd, T. G.: Attribution of climate extreme events, *Nat. Clim. Change*, 5, 725–730, <https://doi.org/10.1038/nclimate2657>, 2015.
- Ulrich, J., Jurado, O. E., Peter, M., Scheibel, M., and Rust, H. W.: Estimating IDF curves consistently over durations with spatial covariates, *Water*, 12, 3119, <https://doi.org/10.3390/w12113119>, 2020.
- 1260 Van den Besselaar, E. J. M., Klein Tank, A. M. G., and Buishand, T. A.: Trends in European precipitation extremes over 1951–2010, *Int. J. Climatol.*, 33, 2682–2689, <https://doi.org/10.1002/joc.3619>, 2013.

- Van Ootegem, L., Verhofstadt, E., Van Herck, K., and Creten, T.: Multivariate pluvial flood damage models, *Environmental Impact Assessment Review*, 54, 91–100, <https://doi.org/10.1016/j.eiar.2015.05.005>, 2015.
- 1265 Van Ootegem, L., Van Herck, K., Creten, T., Verhofstadt, E., Foresti, L., Goudenhoofd, E., Reyniers, M., Delobbe, L., Murla Tuyls, D., and Willems, P.: Exploring the potential of multivariate depth-damage and rainfall-damage models, *Journal of Flood Risk Management*, 11, S916–S929, <https://doi.org/10.1111/jfr3.12284>, 2018.
- Wandel, J.: Starkregen, Deutschland, 29.06.2017, Wettergefahren-Frühwarnung, Center for Disaster Management and Risk Reduction Technology, Karlsruhe, Germany. Available from: http://www.wettergefahren-fruehwarnung.de/Ereignis/20170630_e.html (Accessed 13 August 2021), 2017.
- 1270 Warrach-Sagi, K., Schwitalla, T., Wulfmeyer, V., and Bauer, H.-S.: Evaluation of a climate simulation in Europe based on the WRF–NOAH model system: precipitation in Germany, *Clim. Dyn.*, <https://doi.org/10.1007/s00382-013-1727-7>, 2013.
- Wasko, C., Sharma, A., and Westra, S.: Reduced spatial extent of extreme storms at higher temperatures, *Geophys. Res. Lett.*, 43, 4026–4032, <https://doi.org/10.1002/2016GL068509>, 2016.
- 1275 Werner, P. and Gerstengarbe, F.-W.: Catalog of the general weather situations of Europe, Potsdam Institute for Climate Impact Research (PIK), <https://www.pik-potsdam.de/en/output/publications/pikreports/.files/pr119.pdf>, [online; accessed 10 Nov 2021], 2010.
- Wilhelm, J., Mohr, S., Punge, H. J., Mühr, B., Schmidberger, M., Daniell, J. E., Bedka, K. M., and Kunz, M.: Severe thunderstorms with large hail across Germany in June 2019, *Weather*, 76, 228–237, <https://doi.org/10.1002/wea.3886>, 2021.
- Wilks, D. S.: *Statistical methods in the atmospheric sciences: An introduction – Second Edition*, Academic Press, Elsevier, Burlington, USA, 1280 2006.
- Winschall, A., Pfahl, S., Sodemann, H., and Wernli, H.: Comparison of Eulerian and Lagrangian moisture source diagnostics – The flood event in eastern Europe in May 2010, *Atmos. Chem. Phys.*, 14, 6605–6619, <https://doi.org/10.5194/acp-14-6605-2014>, 2014.
- Winterrath, T., Brendel, C., Hafer, M., Junghänel, T., Klameth, A., Walawender, E., Weigl, E., and Becker, A.: Erstellung einer radargestützten Niederschlagsklimatologie. Berichte des Deutschen Wetterdienstes, Tech. rep., Offenbach am Main, 2017.
- 1285 Winterrath, T., Brendel, C., Hafer, M., Junghänel, T., Klameth, A., Lengfeld, K., Walawender, E., Weigl, E., and Becker, A.: RADKLIM Version 2017.002: Reprocessed quasi gauge-adjusted radar data, 5-minute precipitation sums (YW), https://doi.org/10.5676/DWD/RADKLIM_YW_V2017.002, 2018.
- Wulfmeyer, V., Behrendt, A., Bauer, H.-S., Kottmeier, C., Corsmeier, U., Blyth, A., Craig, G., Schumann, U., Hagen, M., Crewell, C., Di Girolamo, P., Flamant, C., Miller, M., Montani, A., Mobbs, S., Richard, E., Rotach, M., Arpagaus, M., Russchenberg, H., Schlüssel, P., 1290 König, M., V. G., Steinacker, R., Dorninger, M., Turner, D., Weckwerth, T., A., H., and Simmer, C.: The Convective and Orographically-induced Precipitation Study: A Research and Development Project of the World Weather Research Program for improving quantitative precipitation forecasting in low-mountain region., *B. Am. Meteorol. Soc.*, 89, 1469 – 1506, <https://doi.org/10.1175/1520-0477-89.10.1469>, 2008.
- Wulfmeyer, V., Behrendt, A., Kottmeier, C., Corsmeier, U., Barthlott, C., Craig, G. C., Hagen, M., Althausen, D., Aoshima, F., Arpagaus, 1295 M., Bauer, H.-S., Bennett, L., Blyth, A., Brandau, C., Champollion, C., Crewell, S., Dick, G., Di Girolamo, P., Dorninger, M., Dufournet, Y., Eigenmann, R., Engelmann, R., Flamant, C., Foken, T., Gorgas, T., Grzeschik, M., Handwerker, J., Hauck, C., Höller, H., Junkermann, W., Kalthoff, N., Kiemle, C., Klink, S., König, M., Krauss, L., Long, C. N., Madonna, F., Mobbs, S., Neining, B., Pal, S., Peters, G., Pigeon, G., Richard, E., Rotach, M. W., Russchenberg, H., Schwitalla, T., Smith, V., Steinacker, R., Trentmann, J., Turner, D. D., van Baelen, J., Vogt, S., Volkert, H., Weckwerth, T., Wernli, H., Wieser, A., and Wirth, M.: The Convective and Orographically-

- 1300 induced Precipitation Study (COPS): the scientific strategy, the field phase, and research highlights, *Q. J. R. Meteorol. Soc.*, 137, 3–30, <https://doi.org/https://doi.org/10.1002/qj.752>, 2011.
- Wulfmeyer, V., Späth, F., Behrendt, A., Jach, L., Warrach-Sagi, K., Ek, M., Turner, D. D. and Senff, C., Ferguson, C. R., Santanello, J., Lee, T. R., Buban, M., and Verhoef, A.: The GEWEX Land-Atmosphere Feedback Observatory (GLAFO), *GEWEX Quarterly*, 30, 6–11, https://www.gewex.org/gewex-content/files_mf/1583952472Feb2020.pdf, 2020.
- 1305 Yu, C., Li, Z., and Blewitt, G.: Global Comparisons of ERA5 and the Operational HRES Tropospheric Delay and Water Vapor Products With GPS and MODIS, *Earth and Space Science*, 8, <https://doi.org/10.1029/2020ea001417>, 2021.



For this event, land masses are the main sources of moisture uptake with a total contribution of 82.9% study period (29%, whereas only 17.1% June 2017 06 % of the precipitating moisture evaporated over the ocean (of the identified 49.8 UTC to 30 % precipitating moisture; Fig. 9). The eastern European region (around 10°E to 32°E and 37°N to 60°N) is by far the main source of moisture uptake (63.0%). Additionally, the moisture uptake in this region is relatively evenly distributed, ranging from Poland (east of the precipitation event) towards Croatia and Italy, with a maximum moisture uptake of about 4.6 mm per single grid point. Other, but less important, land moisture sources are the western European region (around 12°W to 10°E and 37°N to 60°N), with a contribution of 13.9%, and the northern African region (around 20°W to 32°E and 20°N to 37°N), with a contribution of 5.9%. The oceanic moisture sources are primarily the Mediterranean Sea (11.9%) and Atlantic Ocean (4.6%), but these play a minor role compared to the moisture uptake over land. A similarly important role of moisture recycling from land sources has been found previously for an extreme precipitation event in eastern Europe in May 2010 (Winschall et al., 2014) and for the central European floods in June 2013 (Grams et al., 2014; Kelemen et al., 2016). In the case of the June 2017 event studied here, moisture recycling likely happened on relatively short time scales of 1-2 days, as June 2017 was generally dry, but northeastern Italy, Slovenia, Austria and southeastern Poland were affected by convective precipitation on 28 June. The moistening of the soil due to prior precipitation is thus hypothesised to be an important precondition for the Berlin event. UTC from REGNIE .

For this event, land masses are the main sources of moisture uptake with a total contribution of 82.9% study period (29%, whereas only 17.1% June 2017 06 % of the precipitating moisture evaporated over the ocean (of the identified 49.8 UTC to 30 % precipitating moisture; Fig. 9). The eastern European region (around 10°E to 32°E and 37°N to 60°N) is by far the main source of moisture uptake (63.0%). Additionally, the moisture uptake in this region is relatively evenly distributed, ranging from Poland (east of the precipitation event) towards Croatia and Italy, with a maximum moisture uptake of about 4.6 mm per single grid point. Other, but less important, land moisture sources are the western European region (around 12°W to 10°E and 37°N to 60°N), with a contribution of 13.9%, and the northern African region (around 20°W to 32°E and 20°N to 37°N), with a contribution of 5.9%. The oceanic moisture sources are primarily the Mediterranean Sea (11.9%) and Atlantic Ocean (4.6%), but these play a minor role compared to the moisture uptake over land. A similarly important role of moisture recycling from land sources has been found previously for an extreme precipitation event in eastern Europe in May 2010 (Winschall et al., 2014) and for the central European floods in June 2013 (Grams et al., 2014; Kelemen et al., 2016). In the case of the June 2017 event studied here, moisture recycling likely happened on relatively short time scales of 1-2 days, as June 2017 was generally dry, but northeastern Italy, Slovenia, Austria and southeastern Poland were affected by convective precipitation on 28 June. The moistening of the soil due to prior precipitation is thus hypothesised to be an important precondition for the Berlin event. UTC from REGNIE .

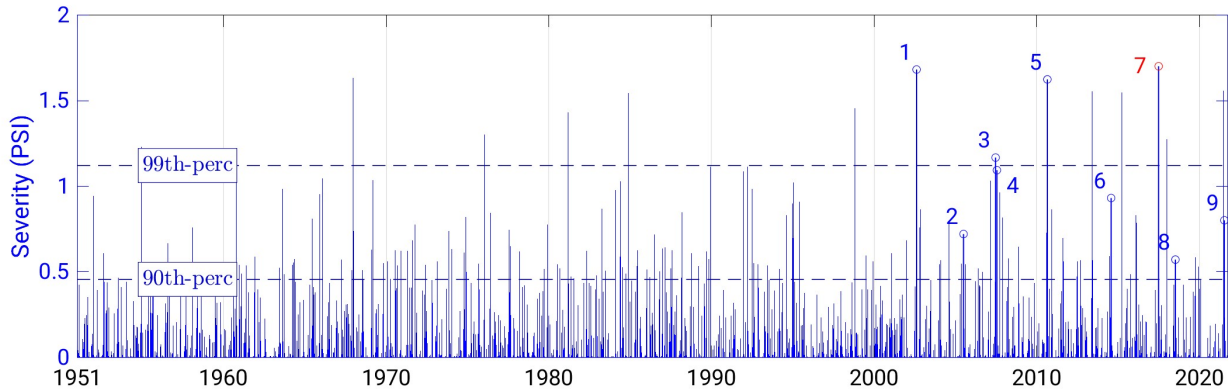


Figure 6. Temporal evolution of the PSI (blue bars). The results are based on REGNIE daily precipitation observations between January 1951 and September 2021. The 99-percentile and 90-percentile of daily PSI values are represented by the dashed blue horizontal lines. Numbered circles highlight nine events analysed in Table 1 or in Fig. 7 as well as other historical events. These are (1) the Saxony floodings on the 12 August 2002; (2) the 29 June 2005 event, affecting Hersbruch and Lohmar; (3) the 21 June 2007 and the (4) 22 July 2007 events affecting Germany in its totality; (5) the 26 August 2010 event in Osnabrueck; (6) the 29 July 2014 event in Muenster and Greven; (7) the 29 June 2017 HPE (red); (8) the 12 July 2018 causing flooding in Berlin; and (9) the Ahr flooding on 14 July 2021.

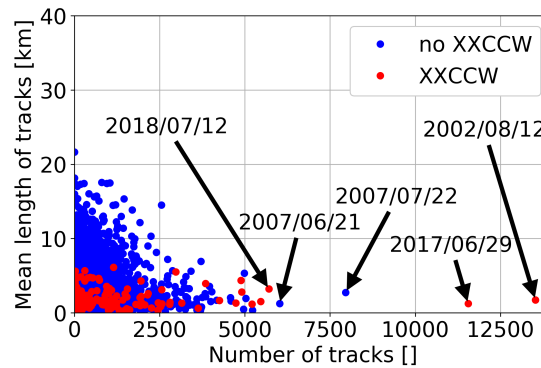


Figure 7. Cell track characteristics (mean length and number of tracks) for the research area Berlin and surroundings for days from 2001 to 2020. Colour coding identifies if days have been classified as weather type 'no prevailing wind direction, cyclonic circulation in 950 and 500 hPa and above-average humidity content of the troposphere - XXCCW' or another type - not XXCCW (Bissolli and Dittmann, 2001). Arrows indicate days with flooding events in Germany.

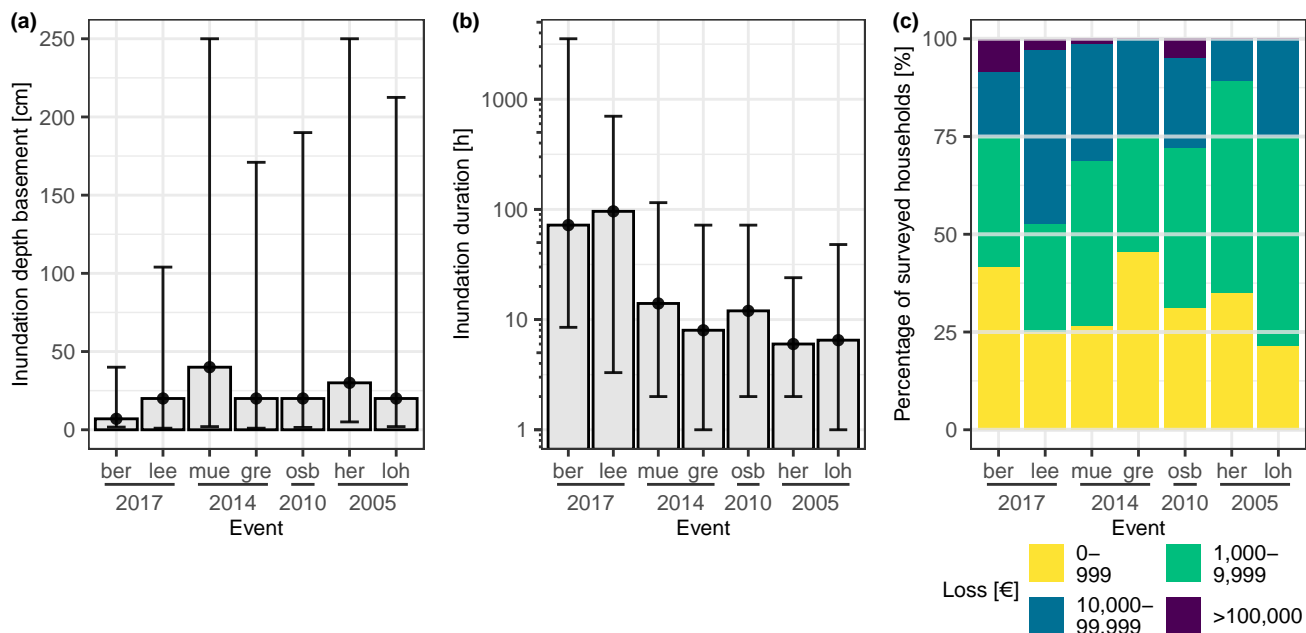


Figure 8. Comparison of (a) inundation depth, (b) inundation duration and (c) building loss between pluvial flood events in seven municipalities as reported in the surveys Berlin-2017 (ber), Leegebruch-2017 (lee), Muenster-2014 (mue), Greven-2014 (gre), Osnabrueck-2010 (osb), Hersbruck-2005 (her), Lohmar-2005 (loh). Points indicate median values, while whiskers show 5 % and 95 % percentiles.

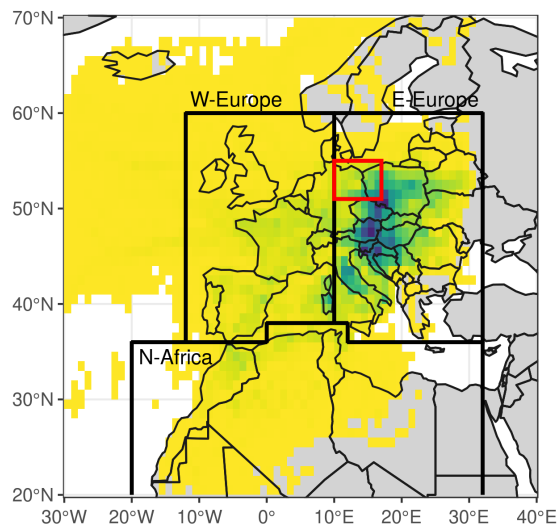


Figure 9. Moisture uptake within the planetary boundary layer, calculated based on Lagrangian backward trajectories using ERA5 reanalysis data. Hourly initialised trajectories on 29 June 2017 (0 UTC to 23 UTC) at the region of heavy precipitation (red box) from 1000 hPa to 200 hPa in steps of 50 hPa and 80 km horizontal distances, going back 240 h in time, are used to compute moisture uptake based on humidity changes, if they are associated with precipitation in the target region.

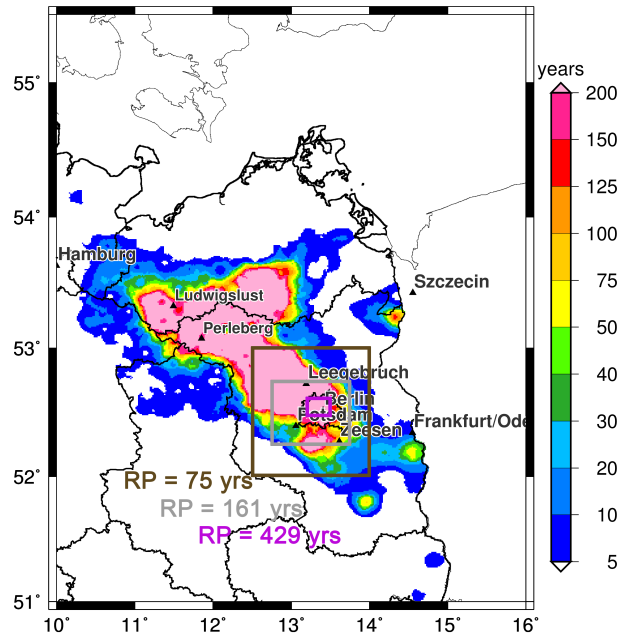


Figure 10. Return periods of the 24-hour precipitation totals based on REGNIE using a Gumbel distribution (Extreme Value Type I; reference period: 1951 – 2020). Note: All return periods above 200 years are shown uniformly in one colour due to statistical uncertainty (see text for more information). Coloured polygons (in pink, grey, brown) including the associated averaged return periods (RP) indicate three different-sized averaging areas explained in Table S2-S2 and in the text.

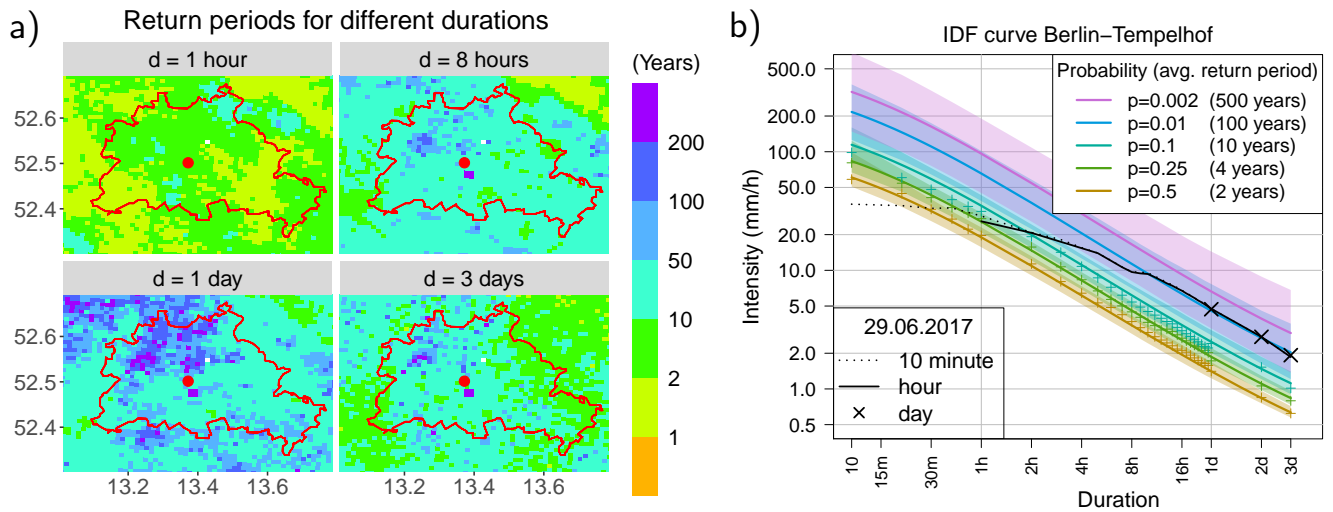


Figure 11. a): Return periods of this event’s intensity from gridded RADKLIM (1 km × 1 km) data using a duration-dependent GEV distribution. Red dot: position of DWD weather station Tempelhof, used to construct the IDF curve in (b). **b):** IDF curves from station-based data. The coloured lines show return periods from the d -GEV model, the black line indicates intensity of the event at on the 29 June 2017 for different temporal measurement resolutions. Empirical quantiles are denoted as coloured "+". 95 % confidence intervals come from 1000-fold bootstrapping.

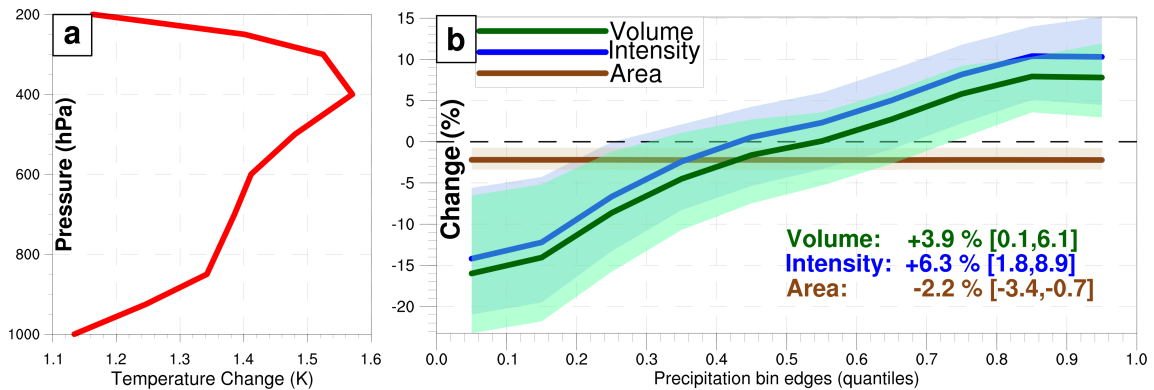


Figure 12. (a) Vertical warming signal and **(b)** response of event precipitation to warming signal. The warming is based on a subset of 17 CMIP6 models. The x-axis in (b) shows precipitation bins which are delineated by quantiles of the precipitation intensity distribution; the changes in area and volume represent the changes associated with precipitation in these bins. Based on the Wilcoxon-Mann-Whitney test, the total changes given within (b) are all statistically significant with at least $p < 0.02$. Shading denotes the 95 % confidence intervals based on 1,000 bootstrap resamples.

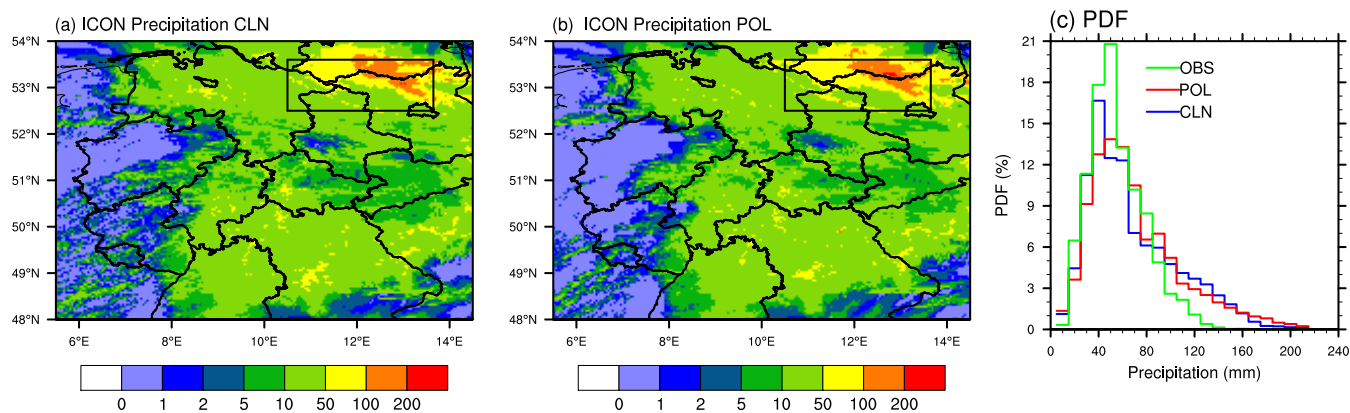


Figure 13. Results from the 635 m ICON simulations. Distribution of precipitation (mm d^{-1}) from (a) the factual CLN simulation and (b) the counterfactual POL simulation. (c) PDF of precipitation intensities in the region of interest denoted by the rectangle in a) and b), for the factual (CLN) and polluted (POL) simulations and the observations (OBS) from the RADKLIM precipitation observations.

Supplementary Material

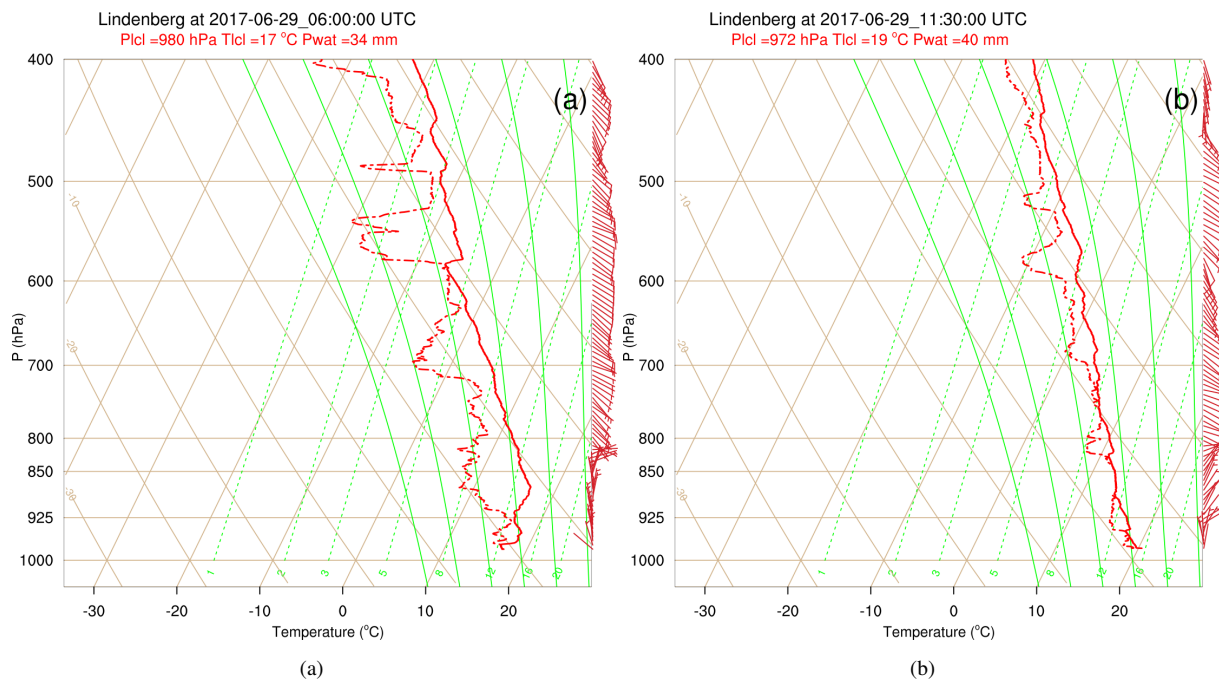


Figure S1. Radiosoundings from Lindenberg (southeast of Berlin), valid at 06 UTC (left) and 12 UTC (middle), 29 June 2017.

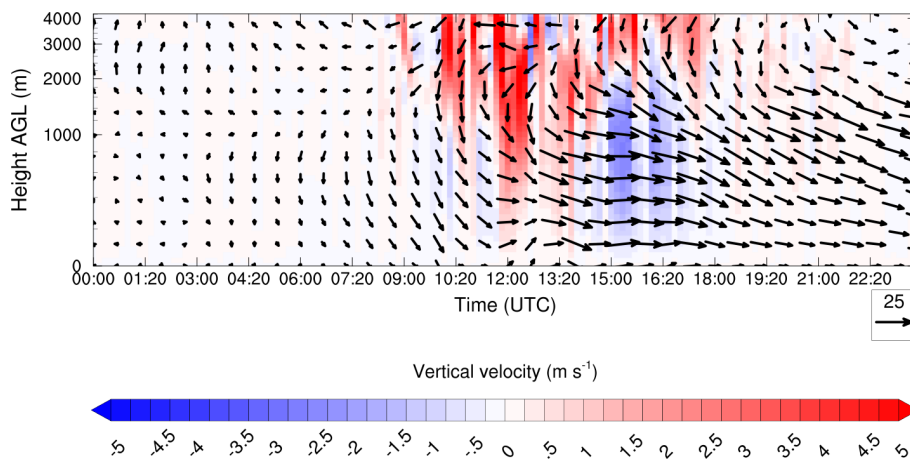


Figure S2. Time-height cross-section of simulated vertical velocities at the same location as in Fig. 4

Table S1. List of the 20 highest 24-hour precipitation totals (mm) in the federal state of Brandenburg (BB), Berlin (BE) and southern Mecklenburg-Western Pomerania (MV) on 29 June 2017 (DWD stations).

ID	Name	Rainfall (mm)	Coordinates
430	Berlin-Tegel (BE)	196.9	52.56°N, 13.32°E
5983	Zeesen (BB)	149.9	52.26°N, 13.62°E
2733	Kremmen-Groß Ziethen (BB)	130.6	52.73°N, 13.01°E
5307	Berge/Prignitz (BB)	124.0	53.24°N, 11.87°E
3205	Marwitz (Wasserwerk) (BB)	113.2	52.66°N, 13.18°E
3196	Marnitz (MV)	112.9	53.32°N, 11.93°E
433	Berlin-Tempelhof (BE)	112.8	52.47°N, 13.40°E
4013	Pritzwalk (BB)	110.0	53.17°N, 12.16°E
2531	Karstädt/Prignitz (BB)	109.2	53.17°N, 11.75°E
2863	Langerwisch (BB)	106.5	52.32°N, 13.07°E
4637	Staaken (BB)	106.0	52.54°N, 13.12°E
7413	Grabow-Stadt (MV)	105.4	53.28°N, 11.56°E
2779	Kuhbier (BB)	103.6	53.15°N, 12.09°E
5555	Thyrow (BB)	103.2	52.25°N, 13.24°E
2472	Jühnsdorf-Blankenfelde (BB)	103.0	52.32°N, 13.39°E
5825	Berge /BB)	102.6	52.62°N, 12.79°E
2637	Klink (MV)	100.4	53.46°N, 12.61°E
400	Berlin-Buch (BE)	99.3	52.63°N, 13.50°E
426	Berlin-Schmöckwitz (BE)	95.2	52.38°N, 13.62°E
4894	Hennigsdorf b. Berlin-Stolpe-Süd (BB)	95.0	52.63°N, 13.23°E

Comparing the return periods of the 29 June 2017 and 14 July 2021 extreme events

Here, we will discuss the 2017 extreme event in the context of the Kreienkamp et al. (2021) study as the events exhibit similarities regarding the local scale and its convective characteristic. It should be noted, however, that Kreienkamp et al. (2021) has been a rapid attribution study which has not gone through peer-review yet. The July 2021 severe precipitation at the Ahr, Erft and Meuse has been an extremely rare event – so rare that estimation of a return period for the combined Ahr and Erft catchment is challenging. Thus, a pooling approach, whereby tiles of equal size in a wider region around the event are used to estimate the return period and the impact of anthropogenic climate change on the event, was applied. Choosing such an approach was based on the assumption that the given event could have occurred anywhere in a wider region around the event. It was found that in any 130x130km tile within the wider region, one such event can be expected every 400 years, which means that several such events would occur in the wider western European region in 400 years.

To put the event we analyse here into the context of Kreienkamp et al. (2021), we compare the return periods of the events. Table S2 gives the return period of the 2017 event, spatially averaged over regions of different sizes (see also Sect. 4.3). The return period of the 2017 event, which has locally quite long return periods, decreases to 75 years when averaged over an area of 11,100 km^2 (100×111 km, yellow box in Figure 4.2), which is still smaller than the area size selected in Kreienkamp et al. (2021). Thus, the 2017 event has a lower return period than the 2021 event on a regional scale.

Table S2. Return period estimates for spatially averaged daily precipitation accumulation for regions of different size. The three regions (pink, grey, brown) are shown in Figure 10.

Region	Latitude [°] south corner	Latitude [°] north corner	Longitude [°] west corner	Longitude [°] east corner	Area size [km^2]	24-hour precipitation [mm]	Return period [years]
pink	52.47	52.62	13.20	13.50	340	134.5	429
grey	52.25	52.75	12.75	13.75	3.720	99.0	161
brown	52.00	53.00	12.50	14.00	11.100	75.7	75

Conditional Event Attribution

CMIP6 models and climate-change signal

The CMIP6 models from which we compute the climate-change signal are shown in Table S3. To compute the climate change signal, we first calculate the mean temperature from the CMIP6 pre-industrial simulations from 1850-1859 across all models for the months of June and July (our event occurs on 29th June) and average over the 0.11° domain (Figure S3). This is then repeated for the years 2007-2016, representative of the present climate. As the CMIP6 historical simulations end in 2014, the years 2015 and 2016 are taken from the SSP245 scenario. The actual choice of scenario here is not relevant, because the divergence between the different scenarios from 2015-2016 is trivial. The difference between the 2007-2016 and the 1850-

1859 climate is then taken. This difference is the basis for creating the pre-industrial boundary conditions from the observed boundary conditions, as described in the main manuscript.

Table S3. CMIP6 GCMs used to compute the climate-change signal used for adjusting the initial and lateral boundary conditions in the conditional event attribution study. The 17 GCMs were selected as they were the only ones for which soil temperature data were also available.

	GCM	Experiment	Institute
1	BCC-CSM2-MR	r1i1p1f1	BCC
2	FGOALS-f3-L	r1i1p1f1	CAS
3	FGOALS-g3	r1i1p1f1	CAS
4	CanESM5	r1i1p1f1	CCCma
5	CMCC-CM2-SR5	r1i1p1f1	CMCC
6	ACCESS-ESM1-5	r1i1p1f1	CSIRO
7	ACCESS-CM2	r1i1p1f1	CSIRO-ARCCSS
8	MPI-ESM1-2-HR	r1i1p1f1	DKRZ
9	EC-Earth3	r1i1p1f1	EC-Earth-Consortium
10	IPSL-CM6A-LR	r1i1p1f1	IPSL
11	MIROC6	r1i1p1f1	MIROC
12	MPI-ESM1-2-LR	r1i1p1f1	MPI-M
13	MRI-ESM2-0	r1i1p1f1	MRI
14	CESM2-WACCM	r1i1p1f1	NCAR
15	NorESM2-LM	r1i1p1f1	NCC
16	NorESM2-MM	r1i1p1f1	NCC
17	KACE-1-0-G	r1i1p1f1	NIMS-KMA

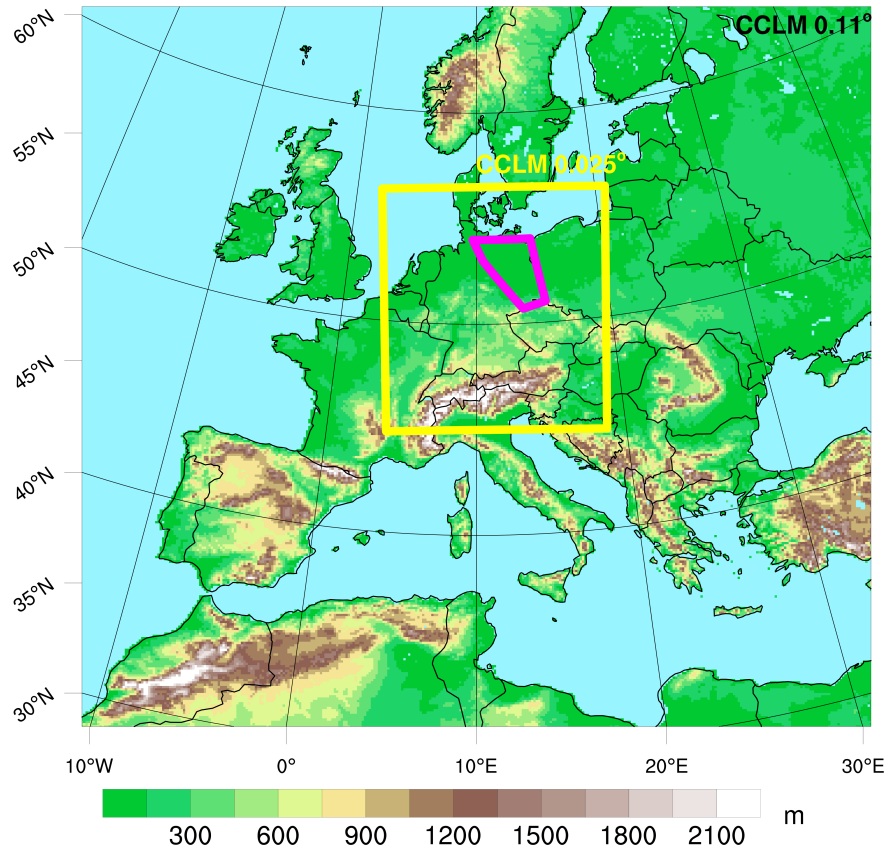


Figure S3. Central 0.11° simulation domain used in the conditional attribution study of Section 4.4 (recall from the description in the main manuscript that the ensemble is created using the domain-shift technique (Rezacova et al., 2009), whereby the boundaries and centre of the 0.11° domain are systematically shifted for each member); shading shows the orography of the 0.11° domain. The 0.025° simulation domain is marked in yellow. The magenta polygon marks the analysis region.

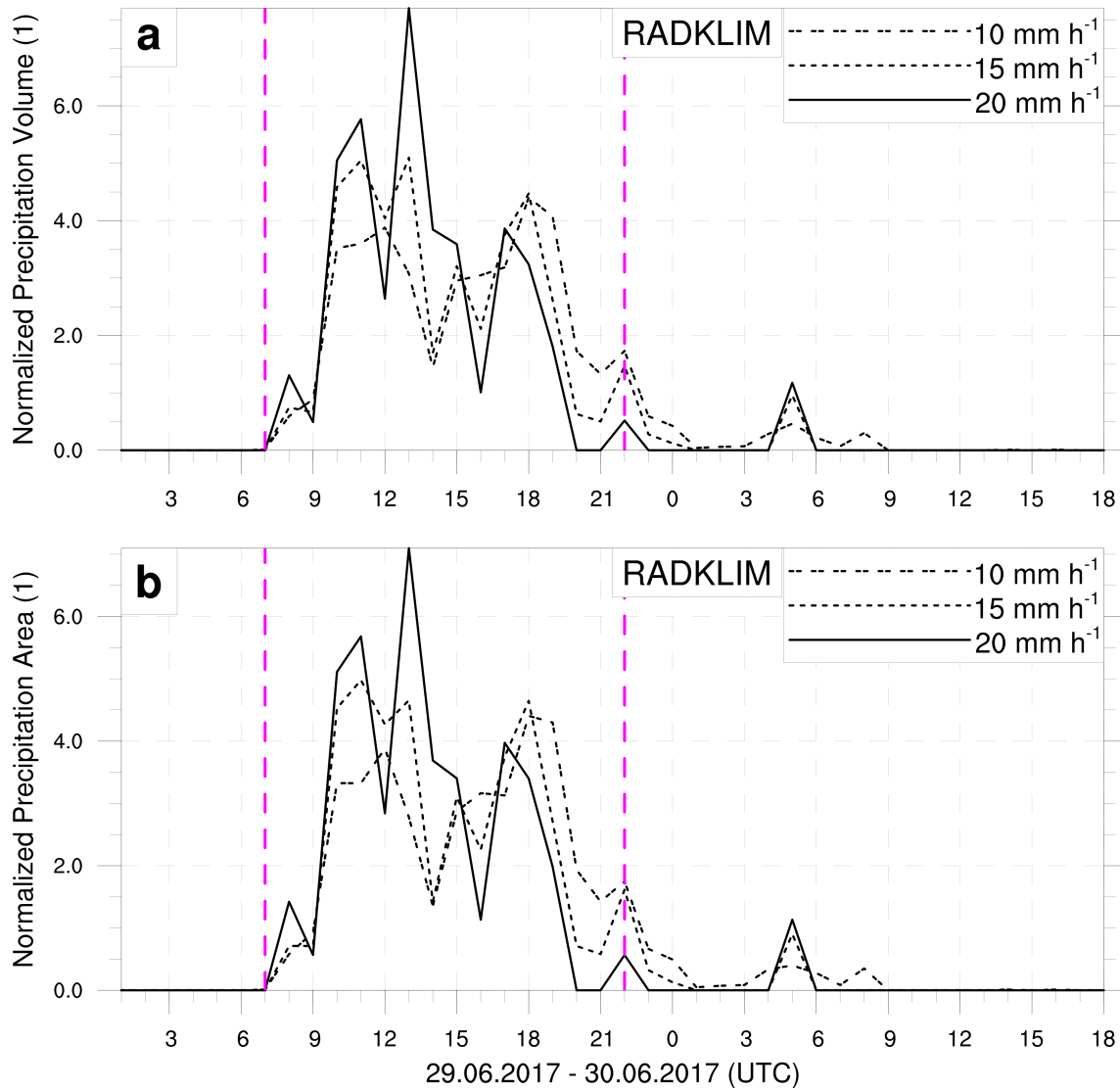


Figure S4. Normalized hourly time series of (a) precipitation volume and (b) precipitation area for different minimum precipitation intensities, based on the radar-based RADKLIM data set (Winterrath et al., 2018). The times series is based on the analysis region marked in Figures S5 and S6. The precipitation intensities denote the minimum precipitation intensities considered for each time series, i.e. for (a), the 10 mm h^{-1} line represents the total precipitation volume based on all grid cells with an hourly rate above 10 mm h^{-1} . The vertical magenta lines mark the time period (i.e. accumulation time) chosen for the analysis presented in Section 4.4 of the main manuscript and below.

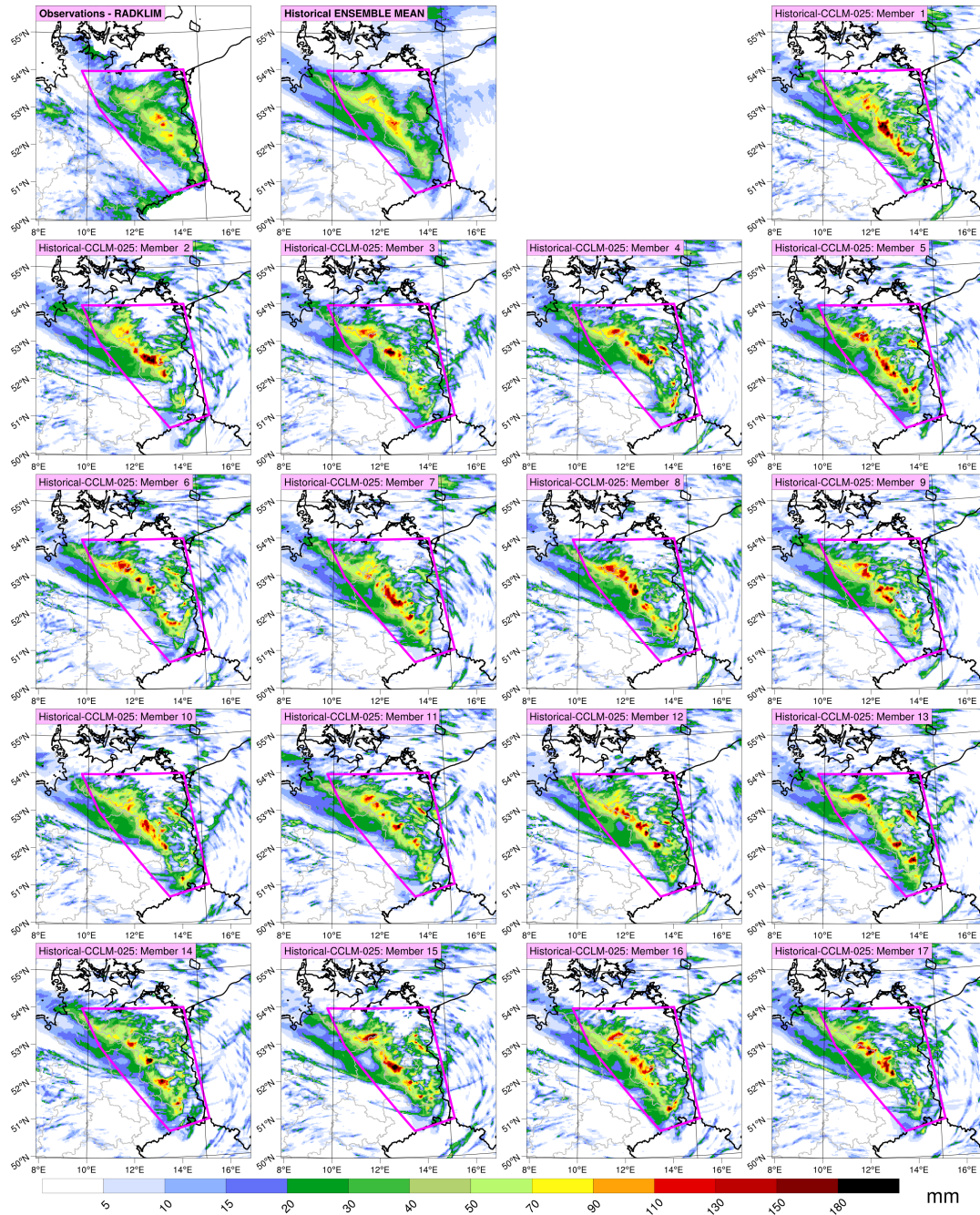


Figure S5. Pre-industrial COSMO-CLM ensemble: event total precipitation accumulations for observations (top left), ensemble mean (top, second from left) and all 17 ensemble members. The magenta box marks the analysis region used in the main manuscript. The accumulation period is as shown in Figure S4. Note that, for fair comparison, the RADKLIM data have been spatially aggregated to the COSMO-CLM 0.025° grid.

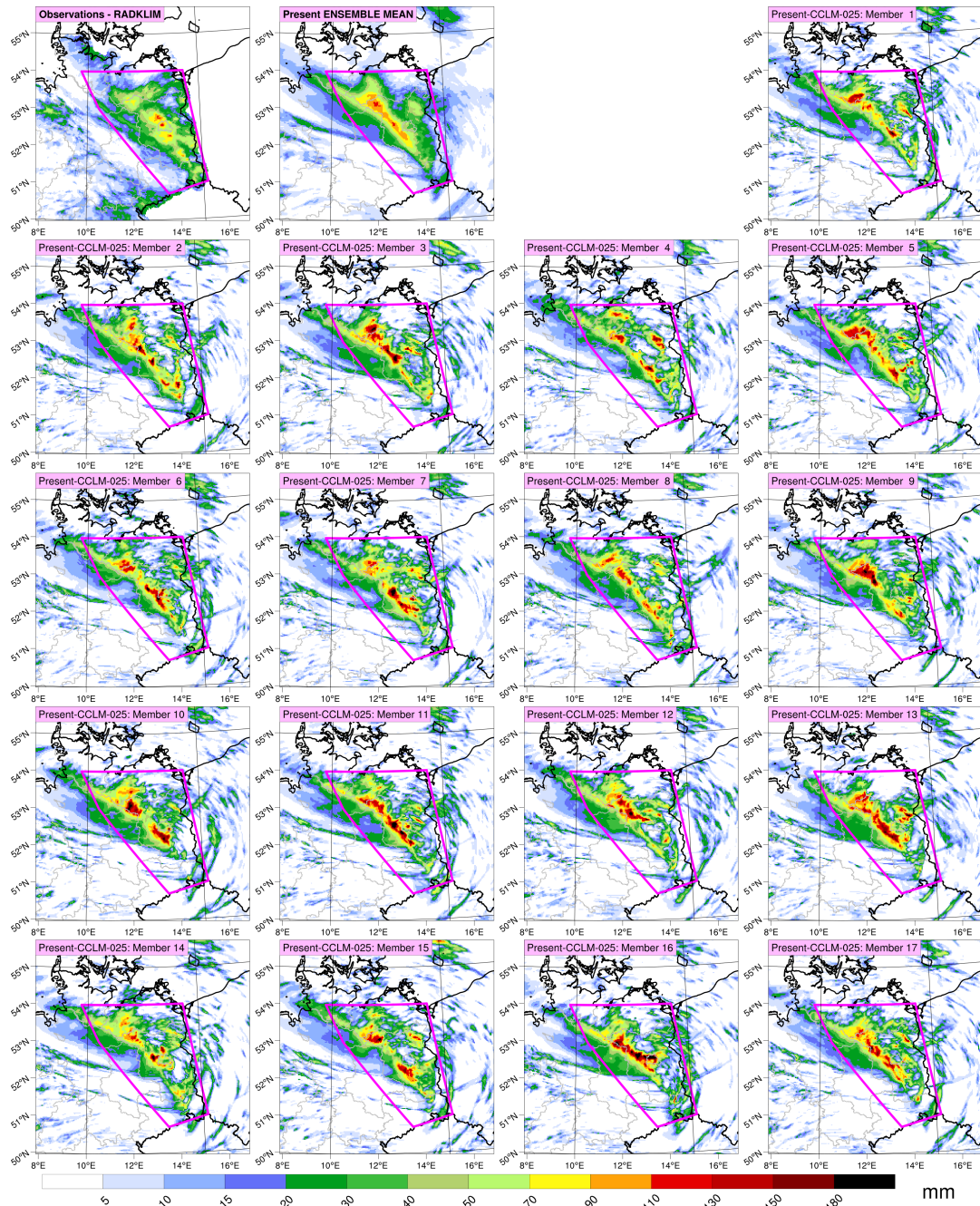


Figure S6. As in Figure S5, except for the present-climate ensemble.